

# Generalization and Robustness Implications in Object-Centric Learning

Andrea Dittadi,<sup>1</sup> Samuele Papa,<sup>1</sup> Michele De Vita,<sup>1</sup>  
Bernhard Schölkopf,<sup>2</sup> Ole Winther,<sup>1</sup> Francesco Locatello<sup>3</sup>

<sup>1</sup>Technical University of Denmark

<sup>2</sup>Max Planck Institute for Intelligent Systems, Tübingen

<sup>3</sup>Amazon

## Abstract

The idea behind object-centric representation learning is that natural scenes can better be modeled as compositions of objects and their relations as opposed to distributed representations. This inductive bias can be injected into neural networks to potentially improve systematic generalization and learning efficiency of downstream tasks in scenes with multiple objects. In this paper, we train state-of-the-art unsupervised models on five common multi-object datasets and evaluate segmentation accuracy and downstream object property prediction. In addition, we study systematic generalization and robustness by investigating the settings where either single objects are out-of-distribution—e.g., having unseen colors, textures, and shapes—or global properties of the scene are altered—e.g., by occlusions, cropping, or increasing the number of objects. From our experimental study, we find object-centric representations to be generally useful for downstream tasks and robust to shifts in the data distribution, especially if shifts affect single objects.

## 1. Introduction

In object-centric representation learning, we exploit the compositional property of natural scenes as inductive bias for neural network architectures, making the assumption that scenes are composed of multiple entities or objects that interact with each other. Informally, the goal is to find useful transformations  $r(\mathbf{x})$  of the input data  $\mathbf{x}$  into a *set* of vector representations, each corresponding to an individual object, without supervision [1–23]. Relying on this inductive bias, object-centric representations are conjectured to be more robust compared to distributed representations [24, 25] and generalize better to novel compositions [26]. Grounding for these claims comes mostly from cognitive psychology and neuroscience [27–29]. Infants learn about the physical properties of objects as entities that behave consistently over time and are able to re-apply their knowledge to new scenarios involving previously unseen objects [27]. Similarly, in complex machine learning downstream tasks like physical modelling and reinforcement learning, it is common to train from the internal representation of a simulator [30, 31] or of a game engine [32, 33] rather than from raw pixels, as higher level variables facilitate learning. Schölkopf et al. [25] argue that learning about objects

---

Correspondence to: [adit@dtu.dk](mailto:adit@dtu.dk). Code written at the Technical University of Denmark.

is a crucial step for *causal representation learning*, as objects can be interpreted as causal variables in a physical system that can be manipulated (i.e., intervened on) independently.

State-of-the-art unsupervised object discovery approaches consist of an encoder learning a representation function  $r$  and a decoder, reconstructing the original input from the elements of  $r(\mathbf{x})$  with shared parameters. The separation of information across objects [26] is commonly evaluated in unsupervised segmentation tasks [9, 11, 14, 20], where quantitative evaluation of segmentation metrics can be performed at validation and test time. As object-centric learning developed recently as a subfield of representation learning, we identify three key hypotheses and design systematic experiments to test them. (1) *The unsupervised learning of objects as pretext task is useful for downstream tasks.* Current state-of-the-art approaches are expected to learn to segment scenes without supervision and also preserve useful information about the object properties in the representation for it to be useful for arbitrary downstream tasks. (2) *Separating objects facilitates strong generalization and robustness to changes affecting a single object.* This assumption stems from recent work in causal representation learning [25]. If objects are akin to causal variables and interventions only act on a single object, the properties of other objects should remain unchanged [25, Sec. 4]. Even out-of-distribution objects with previously unseen properties should be segmented correctly by a network that correctly learned the notion of objects [26] (i.e., “disentangle causal mechanisms” [25]). (3) *Learning about objects improves overall robustness to distribution shifts.* Even if the whole scene is out-of-distribution, for example if all objects are bigger than in the training set, object-centric approaches should be robust thanks to their stronger inductive bias.

In this paper, we put forth three concrete hypotheses that we systematically investigate by re-implementing popular unsupervised object discovery approaches and testing them on five multi-object datasets. In particular: (1) We find that object-centric models achieve good downstream performance on property prediction tasks. We also observe a strong and statistically significant correlation between segmentation metrics, reconstruction error and downstream property prediction performance. (2) We observe that if a single object is out-of-distribution, the overall segmentation performance and the downstream prediction of the in-distribution objects are not strongly impacted. (3) We observe that learning about objects may help with robustness when global properties of the scenes are altered, but this appears to depend on the distribution shift at hand.

## 2. Study design and hypotheses

**Problem definition:** Vanilla deep learning architectures learn distributed representations that do not capture the compositional properties of natural scenes. Even in the literature of disentangled representations [34–40], factors of variations are encoded in a vector representation that is the output of a CNN encoder. This introduces an unnatural ordering of the objects in the scene but also reduces it to a representation of its features rather than the objects that compose it. Formally defining objects is challenging [26] and there is no consensus even outside of machine learning [41, 42]. Greff et al. [26] put forth three properties for object-centric representations: *separation*, i.e., object features in  $r(\mathbf{x})$  do not interact with each other, and each object is individually captured in a single element

of  $r(\mathbf{x})$ ; *common format*, i.e., each element of  $r(\mathbf{x})$  shares the same representational format; and *disentanglement*, i.e., each element of  $r(\mathbf{x})$  is represented in a disentangled format that exposes the factors of variation. In this paper, we consider representations  $r(\mathbf{x})$  that are sets of vectors with each element sharing the representational format. Multi-set would be possible, but for simplicity we do not consider them. We take a pragmatic perspective and focus on two clear desiderata for object-centric approaches:

**Desideratum 1:** *Embodiment of objects.* The representation should contain information about the location of the object and its embodiment in the scene.<sup>1</sup> As we focus on unsupervised object discovery, this translates to segmentation masks. This is related to separation and common format, as the decoder is applied to the elements of  $r(\mathbf{x})$  with shared parameters.

**Desideratum 2:** *Informativeness of the object representation.* Instead of learning disentangled representations of objects, which is challenging even in single-object scenarios [40, 44], we want the representation to contain useful information for downstream tasks, not necessarily in a disentangled format. We define objects through their properties as annotated in the datasets we consider, and predict these properties from the representations. This may not be the only way to define objects (e.g., defining faces and edges as objects and deducing shapes as composition of those). The fact that existing models already learn informative representations is our first hypothesis (see below).

**Design principle:** These desiderata offer well-defined quantitative evaluations for existing object-centric approaches and we want to understand the implications of learning such representations. To this end, we train three state-of-the-art approaches on five datasets, taking best hyperparameter configurations from the respective publications. Assuming these models succeeded in learning an object-centric representation, we investigate the following hypotheses.

**Hypothesis 1:** *The unsupervised learning of objects as pretext task is useful for downstream tasks.* Existing empirical evaluations largely focus on our *Desideratum 1* and evaluate the performance at test time in terms of segmentation metrics. On the other hand, the hope is that the representation would contain useful information for other downstream tasks besides segmentation (*Desideratum 2*). We test this hypothesis by training small downstream prediction models on the frozen object-representations with shared parameters to predict the object properties. We match the predictions to the ground-truth properties with the Hungarian algorithm [45] as done by Locatello et al. [20].

**Hypothesis 2:** *Separating objects facilitates strong generalization and robustness to changes affecting a single object.* One important hypothesis put forth by Schölkopf et al. [25] is that object-representations in deep neural networks should behave akin to causal variables and are therefore an important step in the pursuit of causal representation learning. It is very challenging to validate such a hypothesis in practice, since there is no causal information [46] in the static datasets considered in this field. Our approach relies on measuring violations of the *independent mechanisms* principle [25, 47], stating that “*The causal generative process of a system’s variables is composed of autonomous modules that do not inform or influence each other*”. This implies that interventions on one mechanism should not affect the others. We translate this to the object-centric case as: a change in the properties of one object

---

<sup>1</sup>We use the term *embody* in the sense of “*to make concrete and perceptible*” [43].

should not affect the representation of the other objects. This should hold even if the change leads to an object not being in the training set distribution. We test this hypothesis by (1) evaluating the segmentation of the scene after the distribution shift, and (2) training downstream models to predict object properties, and evaluating them on representations extracted from scenes with one OOD object. More specifically, we test the robustness of this downstream prediction task to changes in the shape, color, or texture (via neural style transfer) of one object.

**Hypothesis 3:** *Learning about objects improves overall robustness.* Early evidence [48] points to the reasonable conjecture that learning object-centric representations biases the network towards learning more robust representations of the overall scene. Intuitively, the notion of objects is an additional inductive bias for the network to exploit to maintain accurate predictions if simple global properties of the scene are altered. We test this hypothesis by training downstream models to predict object properties, and evaluating them on representations of scenes with out-of-distribution global properties. In this case, we test robustness by introducing occlusions, cropping and enlarging the images, and increasing the number of objects in the scene.

### 3. Experimental setup

**Models and datasets.** We implement three state-of-the-art object-centric models—MONet [11], GENESIS [14], and Slot Attention [20]—as well as vanilla variational autoencoders (VAEs) [49, 50] as baselines for distributed representations. As VAE baselines, we use a variant with a broadcast decoder [51] and one with a regular convolutional decoder. See Appendix B for an overview of the models with implementation details. We then collect five popular multi-object datasets: *Multi-dSprites*, *Objects Room*, and *Tetrominoes* from DeepMind’s Multi-Object Datasets collection [52], *CLEVR* [53], and *Shapestacks* [54]. The datasets are described in detail in Appendix C. We train each model on all datasets, using 10 random seeds for object-centric models and 5 for each VAE variant, resulting in 200 models in total.<sup>2</sup> For object-centric models, we use a fixed set of hyperparameters based on the respective publications.

**Segmentation metrics.** We evaluate the segmentation accuracy of object-centric models with the Adjusted Rand Index (ARI) [55], Segmentation Covering (SC) [56], and mean Segmentation Covering (mSC) [14]. For all models, we can additionally evaluate reconstruction quality via the mean squared error (MSE). All these metrics are computed on 5,000 held-out images. We then evaluate the usefulness of the learned representations for downstream tasks, and test the robustness of these representations under two classes of distribution shifts: one where one object goes out-of-distribution, and one where global properties of the scene are changed. Below, we discuss the downstream tasks and distribution shifts considered in this work. We refer to Appendix D for further details.

**Downstream performance.** We evaluate object-centric representations by training downstream models to predict ground-truth object properties from the representations. More

---

<sup>2</sup>Training requires approximately 1 GPU year (NVIDIA V100).



specifically, exploiting the fact that object slots share a common representational format, a single downstream model can be used to predict the properties of each object independently. As in previous work on object property prediction [20], each model simultaneously predicts all features of an object. We use a cross-entropy loss for categorical properties, and MSE for numerical properties. In order to optimize the downstream models, representational slots need to be matched to objects. This is done by computing the similarity between predicted and ground-truth masks, and then solving the assignment problem using the Hungarian algorithm [45] to maximize the total similarity. For property prediction, we use a linear model or an MLP with one hidden layer of size 256. Given a pre-trained object-centric model, we train each downstream model on the representations of 15,000 images from the test split of the relevant dataset. The models are then tested on 5,000 additional images, which may exhibit distribution shifts as discussed below.

**Distribution shifts.** To evaluate generalization to distribution shifts affecting a single object, we systematically induce changes in the color, shape, and texture of objects. To change color, we apply a uniform random shift in RGB values to one random object in the scene, using the available masks. We only do this in the 3 datasets where object color is a categorical variable (CLEVR, Tetrominoes, Shapestacks), as in the other datasets the training distribution covers the entire color space. To test robustness to unseen textures, we apply neural style transfer [57] to one random object in each scene at test time, using *The Great Wave off Kanagawa* as style image. When either a new color or a new texture is introduced, prediction of material (in CLEVR only) and color is not performed. To introduce a new shape, we select images from multi-dSprites that have at most 4 objects (in general, they have up to 5), and add a randomly colored triangle, in a random position, at a random depth in the object stack. In this case, shape prediction does not apply. Finally, to test robustness to global changes in the scene, we change the number of objects at test time (in CLEVR only), introduce occlusions by adding a grey square at a random location, or crop images at the center and restore their original size via bilinear interpolation.

**Limitations of our study.** While we aim to conduct a sound and informative experimental study to answer the research questions presented in the previous sections, inevitably there are limitations regarding datasets, models, and evaluations. Although the datasets considered here vary significantly in complexity and visual properties, they all consist of synthetic images where object properties are independent of each other and independent between objects. Regarding object-centric models, we only focus on autoencoder-based approaches that model a scene as a mixture of components. As official implementations are not always available, and none of the methods in this work has been applied to all the datasets considered here, we re-implement these methods and choose hyperparameters for all datasets following a best-effort approach. Finally, on the evaluation side we only consider the downstream task of object property prediction, and six distribution shifts for assessing generalization.

## 4. Results

In this section, we highlight our findings with plots that are representative of our main results. In Appendix A, we provide the full experimental results with a complete set of plots for

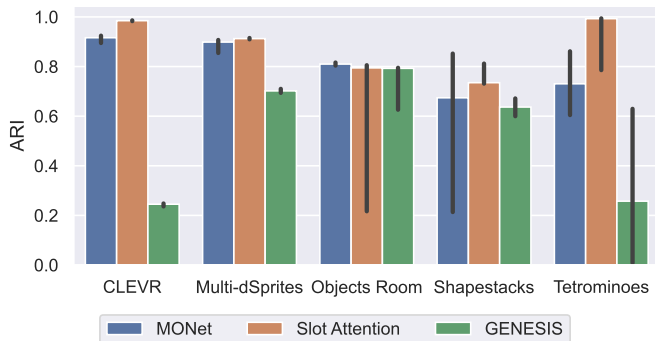


Figure 1: ARI score of all models and datasets, computed on 5,000 test images. Medians and 95% confidence intervals with 10 random seeds.

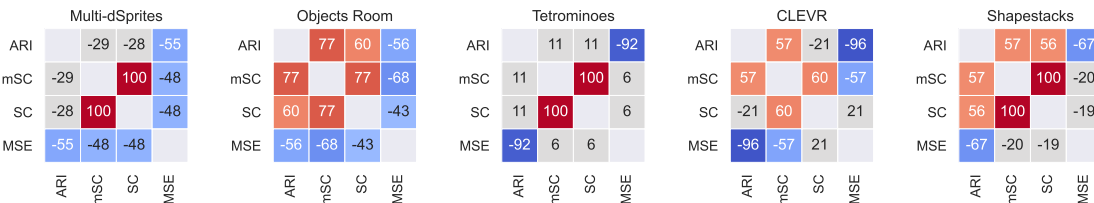


Figure 2: Spearman rank correlations between evaluation metrics across different models and random seeds, reported separately by dataset. The correlations are in the range  $[-100, 100]$  and are color-coded whenever the corresponding p-value is  $< 0.05$ .

different methods and datasets. In Section 4.1 we focus on the different evaluation metrics and the performance we obtained re-training the considered approaches, in Section 4.2 we focus on hypothesis 1, in Section 4.3 on hypothesis 2, and in Section 4.4 on hypothesis 3.

#### 4.1 Learning and evaluating object discovery

Since each of the methods included in our study was originally evaluated only on a subset of the datasets and metrics considered here, we first test how well these models perform.

Fig. 1 shows the segmentation performance of the considered models in terms of ARI score across models, datasets, and random seeds. Fig. 10 in Appendix A provides an overview of the reconstruction MSE and all segmentation metrics. Although these results are in line with published work, we observe substantial differences in the ranking between models depending on the metric. This indicates that these metrics are not equivalent for measuring object discovery.

In Fig. 2, we show rank correlations between metrics on different datasets, aggregating the results from different models. We observe a strong negative correlation between ARI and MSE across models and datasets, which indicates that models that learn to more accurately reconstruct the input tend to better segment objects according to the ARI score. This trend is less consistent for the other segmentation metrics, as MSE significantly correlates

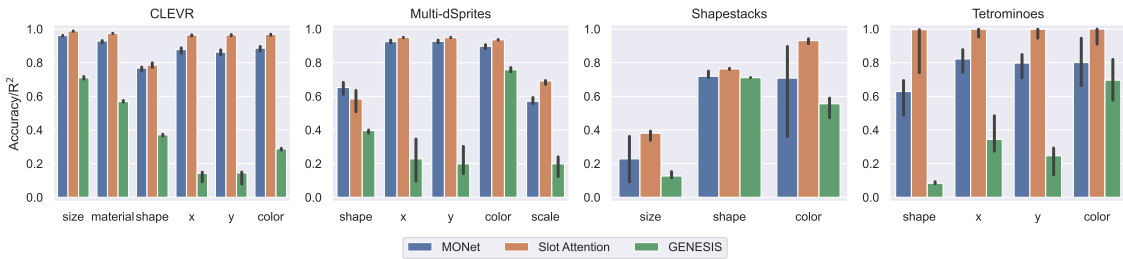


Figure 3: Downstream property prediction using an MLP, for all datasets and models. Medians and 95% confidence intervals with 10 random seeds.

with mSC in only 3 datasets (Multi-dSprites, Objects Room, and CLEVR), and with SC in 2 (Multi-dSprites and Objects Room). SC and mSC measure very similar segmentation notions and therefore are significantly correlated in all datasets, although to a varying extent. However, they correlate with ARI only on 2 and 3 datasets, respectively (the same datasets where they correlate with the MSE).

**Summary:** When reproducing results from the literature, we observe strong differences in performance (and ranking) depending on the chosen evaluation metric. In the tested datasets, we find that ARI (which requires ground-truth segmentation masks to compute) correlates particularly well with MSE (which is unsupervised and provides training signal).

## 4.2 Usefulness for downstream tasks (Hypothesis 1)

To test Hypothesis 1, we first evaluate whether frozen object-centric representations can be used to train downstream classifiers measuring the *Desideratum 2* we put forth in Section 2.

In Fig. 3, we show downstream prediction accuracy or  $R^2$  scores on all datasets and models, when using an MLP as downstream model. Although results vary across datasets and models, accurate prediction of object properties seems to be possible in most of the scenarios considered here. Fig. 12 in Appendix A shows similar results when using a linear downstream model. Interestingly, using a more flexible downstream model (an MLP with one hidden layer of size 256 instead of a linear model) significantly improves downstream prediction performance only in a few cases (Fig. 22 in Appendix A).

Next, we investigate the relationship between downstream performance and evaluation metrics. Fig. 4 shows the Spearman rank correlation of segmentation and reconstruction metrics with test performance of downstream predictors (in terms of accuracy or  $R^2$ , depending on the nature of the object property). For all datasets, downstream performance is strongly correlated with ARI for all object properties, and for both downstream models. On the other hand, SC and mSC exhibit inconsistent trends across datasets. In conclusion, object-centric models that correctly separate objects according to ARI are useful for downstream object property prediction. Downstream prediction metrics of all object properties are also significantly correlated with the reconstruction MSE in all datasets. This is not particularly surprising, since the representation of a model that cannot properly reconstruct the input

CLEVR												Shapestacks							
ARI	93	89	73	92	93	55	95	93	90	94	92	96	ARI	78	40	85	91	84	87
mSC	52	54	72	51	50	91	56	54	61	53	49	54	mSC	22	-4	27	39	31	23
SC	-23	-21	12	-27	-30	47	-24	-24	-12	-27	-32	-25	SC	22	-4	26	39	31	23
MSE	-92	-91	-70	-91	-91	-55	-95	-93	-88	-92	-90	-92	MSE	-64	3	-62	-69	-63	-72
	size - linear	material - linear	shape - linear	x - linear	y - linear	color - linear	size - MLP	material - MLP	shape - MLP	x - MLP	y - MLP	color - MLP	size - linear	shape - linear	color - linear	size - MLP	shape - MLP	color - MLP	

Multi-dSprites										Tetrominoes									
ARI	76	86	86	71	84	60	86	86	91	89	ARI	83	91	82	68	90	92	83	89
mSC	-18	-45	-46	-5	-46	28	-45	-42	-39	-42	mSC	-12	-7	-23	-32	-3	-3	-15	-6
SC	-19	-46	-47	-6	-46	27	-46	-43	-40	-42	SC	-12	-7	-23	-32	-3	-3	-15	-6
MSE	-56	-42	-42	-70	-42	-79	-43	-41	-50	-44	MSE	-92	-91	-93	-61	-95	-93	-92	-83
	shape - linear	x - linear	y - linear	color - linear	scale - linear	shape - MLP	x - MLP	y - MLP	color - MLP	scale - MLP	shape - linear	x - linear	y - linear	color - linear	shape - MLP	x - MLP	y - MLP	color - MLP	

Figure 4: Spearman rank correlations between evaluation metrics and downstream performance, reported separately by dataset, object property, and downstream model. The correlations are in the range  $[-100, 100]$  and are color-coded whenever the corresponding p-value is  $< 0.05$ .

might not contain the information necessary for property prediction. Interestingly, however, the correlation with ARI is generally stronger than the one with MSE, suggesting that ARI might be a more suitable metric for predicting downstream performance.

Finally, we investigate whether object-centric representations are more useful for downstream tasks than unstructured representations. Since in non-object-centric models the representations of the single objects are not readily available, matching objects to representations for downstream property prediction is not trivial. Although this is an inherent limitation of distributed representations in the scenarios considered here, we are nevertheless interested in evaluating the downstream usefulness of such representations. Following Greff et al. [9], we choose a canonical ordering of object properties, and sort objects accordingly when doing property prediction.<sup>3</sup> We then train a downstream model to predict all properties of all objects at once. Note that, unlike the simple slot-wise model we use for object-centric representations, this model also has to learn to sort objects according to the arbitrarily chosen total order. However, on the other hand, it can exploit this order to predict more accurately than random guessing even without using information from the input (this effect is non-negligible only for those properties that are most significant in the order). In Fig. 5, we observe that downstream prediction performance from the distributed representations of

<sup>3</sup>This ordering was chosen by Greff et al. [9] to maximize predictability of the ordering in CLEVR.

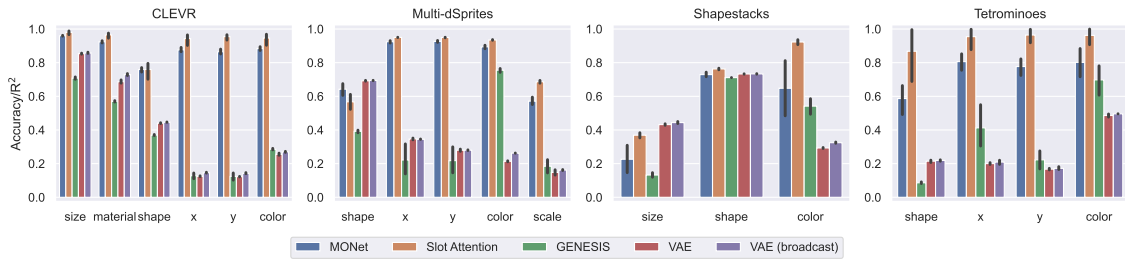


Figure 5: Comparison of downstream property prediction performance for object-centric and distributed representations, using an MLP downstream model. Medians and 95% confidence intervals with 10 random seeds.

VAEs is generally worse than from object-centric representations. Although the comparison is not necessarily fair, these results suggest that object-centric representations are indeed useful for the type of downstream tasks considered here.

**Summary:** Models that accurately segment objects generally allow for good performance in downstream object property prediction. ARI and (to a lesser extent) MSE are consistently correlated with downstream performance. ARI is therefore a promising approach for model selection when masks are available, otherwise MSE can be a useful unsupervised metric. Object-centric representations offer clear advantages over distributed representations in object-centric downstream tasks.

### 4.3 Generalization with one OOD object (Hypothesis 2)

To test Hypothesis 2, we construct settings where a single object is OOD and the others are in distribution. We change the color of one object at random (in CLEVR, Tetrominoes, and Shapestacks), introduce a new shape (in multi-dSprites), or change the object style with neural style transfer (in all datasets). The object-centric models are always trained on the original datasets. Then we train downstream models to predict ground-truth object properties from object-centric representations.

We consider two scenarios for this task: (1) train the predictors on the original datasets and test them on the variants with a modified object, (2) train and test the predictors on these dataset variants. In both cases, we test the predictors on representations that might be inaccurate, because the representation function (encoder) is OOD. However, since in case (2) the downstream model is *trained* under distribution shift, this experiment quantifies the extent to which the representation can still be used by a downstream task that is allowed to adapt to the distribution shift—although the representation might no longer represent objects well, it could still contain useful information for downstream tasks.

For *Desideratum 1*, we observe in Fig. 6 that in terms of ARI the models are generally robust to distribution shifts affecting a single object. Introducing a new color or a new shape does not seem to affect segmentation quality, while changing the texture of an object via neural style transfer in some cases leads to a drop in the ARI score. One exception is Slot

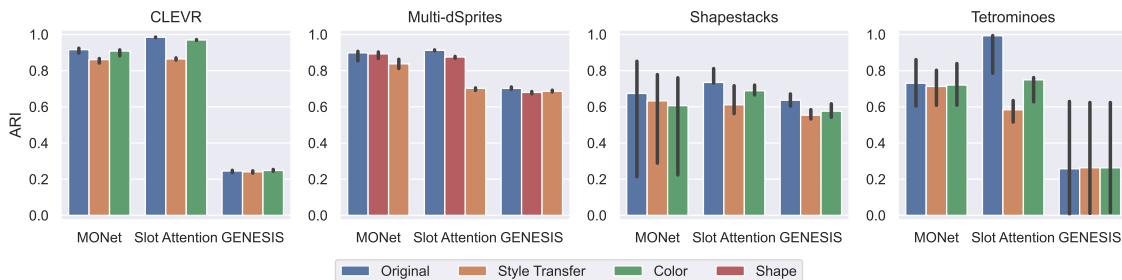


Figure 6: Effect of interventions on a single object on the ARI score. Medians and 95% confidence intervals with 10 random seeds.

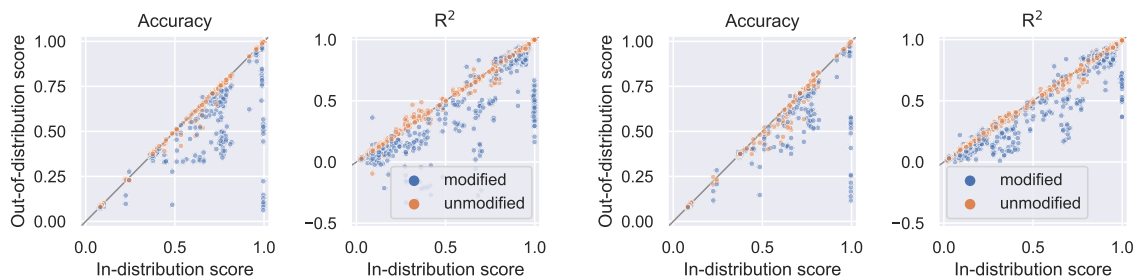


Figure 7: **In-distribution vs OOD downstream performance** for each object property, across datasets and models, when only one object has been altered. The average performance on in-distribution (unmodified) and out-of-distribution (modified) objects is shown in different colors. Metrics: accuracy for categorical attributes,  $R^2$  for numerical attributes. **Left two plots:** training the downstream model on the original training set. **Right two plots:** retraining it on the OOD sets (test performance is always reported on held-out data points).

Attention on most datasets, where the ARI score on the training distribution is often higher than the other models but both a new color and a new texture lead to a significant drop in performance (although the final score is still comparable with the scores of the other models). The SC and mSC metrics show similar but less pronounced trends (see Fig. 14 in Appendix A). From these results we conclude that the encoder is partially able to discover objects even under distribution shifts at test time, and that one OOD object largely does not affect the discovery of the in-distribution objects.

For *Desideratum 2*, we observe in Fig. 7 (left) that, across models, datasets, and downstream models, the performance of property prediction for objects that underwent distribution shifts (unseen color, shape, or texture) is significantly worse than the average performance in the original dataset, whereas prediction of in-distribution objects is largely unaffected. This is in agreement with Hypothesis 2, in that interventions on one object do not affect the representation of other objects. More detailed results are shown in Fig. 16 in Appendix A. In Fig. 7 (right) we show that, if we allow retraining of downstream tasks, downstream property prediction of in-distribution objects is still robust. However, while the prediction performance of OOD objects improves, it is still significantly worse than for in-distribution

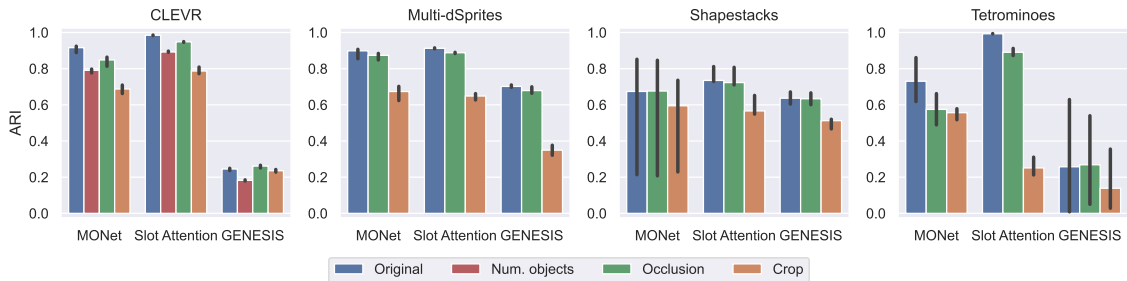


Figure 8: Effect of interventions on global scene properties on the ARI score. Medians and 95% confidence intervals with 10 random seeds.

objects. This suggests that the distribution shifts introduced here do not only affect the downstream model, but also the representation itself. More detailed results are shown in Fig. 18 in Appendix A. While in principle we observe a similar trend for the VAE baseline (see Fig. 20 in Appendix A), its performance is generally too low for a definitive conclusion to be drawn.

**Summary:** In terms of *Desideratum 1*, the considered models appear to be relatively robust to distribution shifts affecting a single object, although interventions on object texture generally lead to a slight drop in performance. Downstream property prediction is largely unaffected for objects that are in distribution, but we generally observe significantly reduced performance for OOD objects. Finally, retraining downstream models on the OOD objects only marginally improves the prediction accuracy, indicating that the encoder is responsible for this performance drop.

#### 4.4 Robustness to transformations changing global properties (Hypothesis 3)

Finally, we investigate how robust object-centric models are to transformations changing the global properties of a scene at test time. Here, we consider variants of the datasets with occlusions (a grey patch is added to the image at a random location), cropping (crop the center of the image and upsample to restore the original size), or increasing the number of objects. Occlusion and cropping are applied to all datasets, while the study on number of objects is only performed on CLEVR. We train downstream predictors on the original datasets and report their test performance on the dataset variants with OOD global properties. As before, we also report results of downstream models retrained on the OOD datasets.

For *Desideratum 1*, Fig. 8 shows that in terms of ARI the models are generally only marginally affected by occlusion, but cropping often leads to a more significant degradation in segmentation quality. In CLEVR, increasing the number of objects leads to lower ARI scores as well, but not as significantly as when cropping. These trends persist when considering SC and mSC, but appear less pronounced and less consistent across datasets (see Fig. 15 in Appendix A for complete results).

For *Desideratum 2*, we train a downstream predictor on the original dataset and test it on scenes with altered global properties. Fig. 9 (left) shows that altering global properties of

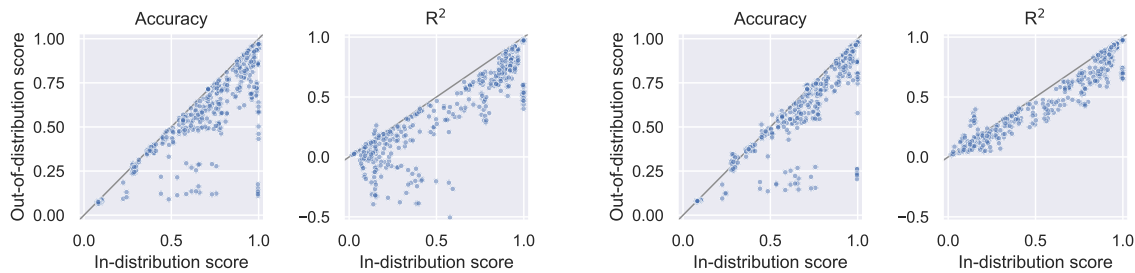


Figure 9: **In-distribution vs OOD downstream performance** for each object property, across datasets and models, when global properties of the scene are altered. Metrics: accuracy for categorical attributes,  $R^2$  for numerical attributes. **Left two plots:** training the downstream model on the original training set. **Right two plots:** retraining it on the OOD sets (test performance is always reported on held-out data).

the scene generally has a negative effect on downstream property prediction. However, this is comparable to the effect of changing one object on property prediction of the object that is OOD. More detailed results are shown in Fig. 17 in Appendix A. Even if we retrain a downstream predictor on the datasets with altered global properties keeping the representation frozen, we observe in Fig. 9 (right) that, as for OOD objects in the single-OOD-object scenario, property prediction performance improves but does not reach the corresponding results on the training set. More detailed results are shown in Fig. 19 in Appendix A.

**Summary:** With the exception of cropping on Multi-dSprites, the tested alterations of the global properties of the scene have limited impact on object-centric representations (often within error bars), but the usefulness for downstream tasks clearly decreases. From these results we conjecture that the robustness of object-centric learning may significantly depend on the task and distribution shift.

## 5. Additional related work

Recent years have seen a number of systematic studies on disentangled representation learning [40, 58–60], some of which focusing on the implications of disentanglement in generalization [61–64]. In the context of object-centric models, Engelcke et al. [65] investigate their reconstruction bottlenecks to understand how these models can separate objects from the input in an unsupervised manner. In contrast, we specifically test some key implications of learning object-centric representations.

Object-centric models can be classified according to their approach to separating the objects at a representational level [26]. In models that use *instance slots* [5, 9, 20, 66–76], each slot is used to represent a different part of the input. This introduces a routing problem, because all slots are identical but they cannot all represent the same object, so a mechanism needs to be introduced to allow slots to communicate with each other. In models based on *sequential slots* [3, 6, 7, 11, 12, 14, 16, 22], the representational slots are computed in a sequential fashion, which solves the routing problem and allows to dynamically change the number of



slots, but introduces possibly unwanted dependencies between slots. Finally, in models based on *spatial slots* [4, 8, 17, 18, 21, 23, 77], a spatial coordinate is associated with each slot, introducing a dependency between slot and spatial location. In this work, we focus on three scene-mixture models as representative examples of approaches based on instance slots (Slot Attention) and sequential slots (MONet and GENESIS), and leave the investigation of other classes of methods for future work.

## 6. Conclusions

In this paper, we identify three key hypotheses in object-centric representation learning: learning about objects is useful for downstream tasks, it facilitates strong generalization, and it improves overall robustness to distribution shifts. To investigate these hypotheses, we re-implement and systematically evaluate state-of-the-art unsupervised object-centric learners on a suite of five common multi-object datasets. We find that object-centric representations are generally useful for downstream object property prediction, and downstream performance is strongly correlated with segmentation quality and reconstruction error. Regarding generalization, we observe that when a single object undergoes distribution shifts the overall segmentation quality and downstream performance for in-distribution objects is largely unaffected. Finally, we find that representing a scene as a composition of objects may be helpful even under distribution shifts affecting global properties of the scene, although this may depend on the corruption at hand.

An interesting avenue for future work is to continue our systematic investigation of object-centric learning on more complex data with diverse textures, as well as a wider array of downstream tasks. Furthermore, while we limit our study to unsupervised object discovery, it would be relevant to consider methods that leverage some form of supervision when learning about objects.

## Acknowledgements

We would like to thank Thomas Brox and Frederik Träuble for the helpful comments.

## References

- [1] Volodymyr Mnih, Nicolas Heess, Alex Graves, et al. Recurrent models of visual attention. In *Advances in neural information processing systems*, pages 2204–2212, 2014.
- [2] Karol Gregor, Ivo Danihelka, Alex Graves, Danilo Rezende, and Daan Wierstra. Draw: A recurrent neural network for image generation. In *International Conference on Machine Learning*, pages 1462–1471. PMLR, 2015.
- [3] SM Ali Eslami, Nicolas Heess, Theophane Weber, Yuval Tassa, David Szepesvari, Geoffrey E Hinton, et al. Attend, infer, repeat: Fast scene understanding with generative models. In *Advances in Neural Information Processing Systems*, pages 3225–3233, 2016.

- [4] Charlie Nash, SM Ali Eslami, Chris Burgess, Irina Higgins, Daniel Zoran, Theophane Weber, and Peter Battaglia. The multi-entity variational autoencoder. In *Neural Information Processing Systems (NeurIPS) Workshop on Learning Disentangled Representations: from Perception to Control*, 2017.
- [5] Klaus Greff, Sjoerd van Steenkiste, and Jürgen Schmidhuber. Neural expectation maximization. In *Proceedings of the 31st International Conference on Neural Information Processing Systems*, pages 6694–6704, 2017.
- [6] Adam R Kosiorek, Hyunjik Kim, Ingmar Posner, and Yee Whye Teh. Sequential attend, infer, repeat: Generative modelling of moving objects. *arXiv preprint arXiv:1806.01794*, 2018.
- [7] Karl Stelzner, Robert Peharz, and Kristian Kersting. Faster Attend-Infer-Repeat with Tractable Probabilistic Models. In Kamalika Chaudhuri and Ruslan Salakhudinov, editors, *Proceedings of the 36th International Conference on Machine Learning*, volume 97, pages 5966–5975. PMLR, June 2019.
- [8] Eric Crawford and Joelle Pineau. Spatially invariant unsupervised object detection with convolutional neural networks. In *Proceedings of the AAAI Conference on Artificial Intelligence*, volume 33, pages 3412–3420, 2019.
- [9] Klaus Greff, Raphaël Lopez Kaufman, Rishabh Kabra, Nick Watters, Christopher Burgess, Daniel Zoran, Loic Matthey, Matthew Botvinick, and Alexander Lerchner. Multi-object representation learning with iterative variational inference. In *International Conference on Machine Learning*, pages 2424–2433. PMLR, 2019.
- [10] Jinyang Yuan, Bin Li, and Xiangyang Xue. Generative modeling of infinite occluded objects for compositional scene representation. In *International Conference on Machine Learning*, pages 7222–7231, 2019.
- [11] Christopher P Burgess, Loic Matthey, Nicholas Watters, Rishabh Kabra, Irina Higgins, Matt Botvinick, and Alexander Lerchner. Monet: Unsupervised scene decomposition and representation. *arXiv preprint arXiv:1901.11390*, 2019.
- [12] Jannik Kossen, Karl Stelzner, Marcel Hussing, Claas Voelcker, and Kristian Kersting. Structured object-aware physics prediction for video modeling and planning. *arXiv preprint arXiv:1910.02425*, 2019.
- [13] Andrea Dittadi and Ole Winther. LAVAE: Disentangling Location and Appearance. *arXiv preprint arXiv:1909.11813*, 2019.
- [14] Martin Engelcke, Adam R. Kosiorek, Oiwi Parker Jones, and Ingmar Posner. GENESIS: Generative Scene Inference and Sampling with Object-Centric Latent Representations. In *ICLR 2020*, 2020.
- [15] Marissa A Weis, Kashyap Chitta, Yash Sharma, Wieland Brendel, Matthias Bethge, Andreas Geiger, and Alexander S Ecker. Unmasking the inductive biases of unsupervised object representations for video sequences. *arXiv preprint arXiv:2006.07034*, 2020.

- [16] Julius von Kügelgen, Ivan Ustyuzhaninov, Peter Gehler, Matthias Bethge, and Bernhard Schölkopf. Towards causal generative scene models via competition of experts. In *ICLR 2020 Workshops*, 2020.
- [17] Jindong Jiang\*, Sepehr Janghorbani\*, Gerard De Melo, and Sungjin Ahn. Scalor: Generative world models with scalable object representations. In *International Conference on Learning Representations*, 2020.
- [18] Zhixuan Lin, Yi-Fu Wu, Skand Vishwanath Peri, Weihao Sun, Gautam Singh, Fei Deng, Jindong Jiang, and Sungjin Ahn. SPACE: Unsupervised Object-Oriented Scene Representation via Spatial Attention and Decomposition. In *ICLR 2020*, 2020.
- [19] Chang Chen, Fei Deng, and Sungjin Ahn. Learning to infer 3d object models from images. *arXiv preprint arXiv:2006.06130*, 2020.
- [20] Francesco Locatello, Dirk Weissenborn, Thomas Unterthiner, Aravindh Mahendran, Georg Heigold, Jakob Uszkoreit, Alexey Dosovitskiy, and Thomas Kipf. Object-centric learning with slot attention. *arXiv preprint arXiv:2006.15055*, 2020.
- [21] Eric Crawford and Joelle Pineau. Exploiting spatial invariance for scalable unsupervised object tracking. In *Proceedings of the AAAI Conference on Artificial Intelligence*, volume 34, pages 3684–3692, 2020.
- [22] Martin Engelcke, Oiwi Parker Jones, and Ingmar Posner. GENESIS-V2: Inferring Unordered Object Representations without Iterative Refinement. *arXiv preprint arXiv:2104.09958*, 2021.
- [23] Fei Deng, Zhuo Zhi, Donghun Lee, and Sungjin Ahn. Generative scene graph networks. In *International Conference on Learning Representations*, 2021.
- [24] Yoshua Bengio, Aaron Courville, and Pascal Vincent. Representation learning: A review and new perspectives. *IEEE Transactions on Pattern Analysis and Machine Intelligence*, 35(8):1798–1828, 2013.
- [25] Bernhard Schölkopf, Francesco Locatello, Stefan Bauer, Nan Rosemary Ke, Nal Kalchbrenner, Anirudh Goyal, and Yoshua Bengio. Toward causal representation learning. *Proceedings of the IEEE*, 109(5):612–634, 2021.
- [26] Klaus Greff, Sjoerd van Steenkiste, and Jürgen Schmidhuber. On the binding problem in artificial neural networks. *arXiv preprint arXiv:2012.05208*, 2020.
- [27] Stanislas Dehaene. *How We Learn: Why Brains Learn Better than Any Machine ... for Now*. Viking, New York, 2020.
- [28] Elizabeth S. Spelke. Principles of object perception. *Cognitive Science*, 14:29–56, 1990. ISSN 0364-0213. doi: 10.1016/0364-0213(90)90025-R.
- [29] Ernő Téglás, Edward Vul, Vittorio Girotto, Michel Gonzalez, Joshua B. Tenenbaum, and Luca L. Bonatti. Pure Reasoning in 12-Month-Old Infants as Probabilistic Inference. *Science*, 332:1054–1059, May 2011. ISSN 0036-8075, 1095-9203. doi: 10.1126/science.1196404.

- [30] Peter Battaglia, Razvan Pascanu, Matthew Lai, Danilo Jimenez Rezende, and koray kavukcuoglu. Interaction networks for learning about objects, relations and physics. In D. Lee, M. Sugiyama, U. Luxburg, I. Guyon, and R. Garnett, editors, *Advances in Neural Information Processing Systems*, volume 29. Curran Associates, Inc., 2016.
- [31] Alvaro Sanchez-Gonzalez, Jonathan Godwin, Tobias Pfaff, Rex Ying, Jure Leskovec, and Peter Battaglia. Learning to Simulate Complex Physics with Graph Networks. In *International Conference on Machine Learning*, pages 8459–8468. PMLR, November 2020.
- [32] Oriol Vinyals, Igor Babuschkin, Wojciech M. Czarnecki, Michaël Mathieu, Andrew Dudzik, Junyoung Chung, David H. Choi, Richard Powell, Timo Ewalds, Petko Georgiev, Junhyuk Oh, Dan Horgan, Manuel Kroiss, Ivo Danihelka, Aja Huang, Laurent Sifre, Trevor Cai, John P. Agapiou, Max Jaderberg, Alexander S. Vezhnevets, Rémi Leblond, Tobias Pohlen, Valentin Dalibard, David Budden, Yury Sulsky, James Molloy, Tom L. Paine, Caglar Gulcehre, Ziyu Wang, Tobias Pfaff, Yuhuai Wu, Roman Ring, Dani Yogatama, Dario Wünsch, Katrina McKinney, Oliver Smith, Tom Schaul, Timothy Lillicrap, Koray Kavukcuoglu, Demis Hassabis, Chris Apps, and David Silver. Grandmaster level in StarCraft II using multi-agent reinforcement learning. *Nature*, 575:350–354, November 2019. ISSN 1476-4687. doi: 10.1038/s41586-019-1724-z.
- [33] OpenAI, Christopher Berner, Greg Brockman, Brooke Chan, Vicki Cheung, Przemysław Dębniak, Christy Dennison, David Farhi, Quirin Fischer, Shariq Hashme, Chris Hesse, Rafal Józefowicz, Scott Gray, Catherine Olsson, Jakub Pachocki, Michael Petrov, Henrique P. d O. Pinto, Jonathan Raiman, Tim Salimans, Jeremy Schlatter, Jonas Schneider, Szymon Sidor, Ilya Sutskever, Jie Tang, Filip Wolski, and Susan Zhang. Dota 2 with Large Scale Deep Reinforcement Learning. *arXiv:1912.06680 [cs, stat]*, 2019.
- [34] Irina Higgins, Loic Matthey, Arka Pal, Christopher Burgess, Xavier Glorot, Matthew Botvinick, Shakir Mohamed, and Alexander Lerchner. beta-VAE: Learning basic visual concepts with a constrained variational framework. In *International Conference on Learning Representations*, 2017.
- [35] Hyunjik Kim and Andriy Mnih. Disentangling by factorising. In *International Conference on Machine Learning*, 2018.
- [36] Tian Qi Chen, Xuechen Li, Roger Grosse, and David Duvenaud. Isolating sources of disentanglement in variational autoencoders. In *Advances in Neural Information Processing Systems*, 2018.
- [37] Karl Ridgeway and Michael C Mozer. Learning deep disentangled embeddings with the f-statistic loss. In *Advances in Neural Information Processing Systems*, 2018.
- [38] Abhishek Kumar, Prasanna Sattigeri, and Avinash Balakrishnan. Variational inference of disentangled latent concepts from unlabeled observations. In *International Conference on Learning Representations*, 2018.

- [39] Cian Eastwood and Christopher KI Williams. A framework for the quantitative evaluation of disentangled representations. In *International Conference on Learning Representations*, 2018.
- [40] Francesco Locatello, Stefan Bauer, Mario Lucic, Sylvain Gelly, Bernhard Schölkopf, and Olivier Bachem. Challenging common assumptions in the unsupervised learning of disentangled representations. In *International Conference on Machine Learning*, 2019.
- [41] Brian Cantell Smith. *On the origin of objects*. MIT Press, 1998.
- [42] Edwin James Green. A theory of perceptual objects. *Philosophy and Phenomenological Research*, 99(3):663–693, 2019.
- [43] Embody. In *Merriam-Webster’s Collegiate Dictionary*. 2020.
- [44] Francesco Locatello, Stefan Bauer, Mario Lucic, Gunnar Rätsch, Sylvain Gelly, Bernhard Schölkopf, and Olivier Bachem. A sober look at the unsupervised learning of disentangled representations and their evaluation. *Journal of Machine Learning Research (JMLR)*, 2020.
- [45] Harold W Kuhn. The Hungarian method for the assignment problem. *Naval research logistics quarterly*, 2(1-2):83–97, 1955.
- [46] Kexin Yi, Chuang Gan, Yunzhu Li, Pushmeet Kohli, Jiajun Wu, Antonio Torralba, and Joshua B Tenenbaum. Clevrer: Collision events for video representation and reasoning. In *International Conference on Learning Representations*, 2019.
- [47] Bernhard Schölkopf, Dominik Janzing, Jonas Peters, Eleni Sgouritsa, Kun Zhang, and Joris Mooij. On causal and anticausal learning. In *International Conference on Machine Learning*, 2012.
- [48] Rob Romijnders, Aravindh Mahendran, Michael Tschannen, Josip Djolonga, Marvin Ritter, Neil Houlsby, and Mario Lucic. Representation learning from videos in-the-wild: An object-centric approach. In *Proceedings of the IEEE/CVF Winter Conference on Applications of Computer Vision*, pages 177–187, 2021.
- [49] Diederik P Kingma and Max Welling. Auto-encoding variational Bayes. In *International Conference on Learning Representations*, 2014.
- [50] Danilo Jimenez Rezende, Shakir Mohamed, and Daan Wierstra. Stochastic back-propagation and approximate inference in deep generative models. *arXiv preprint arXiv:1401.4082*, 2014.
- [51] Nicholas Watters, Loic Matthey, Christopher P Burgess, and Alexander Lerchner. Spatial broadcast decoder: A simple architecture for learning disentangled representations in vaes. *arXiv preprint arXiv:1901.07017*, 2019.
- [52] Rishabh Kabra, Chris Burgess, Loic Matthey, Raphael Lopez Kaufman, Klaus Greff, Malcolm Reynolds, and Alexander Lerchner. Multi-object datasets, 2019. URL <https://github.com/deepmind/multi-object-datasets/>.

- [53] Justin Johnson, Bharath Hariharan, Laurens Van Der Maaten, Li Fei-Fei, C Lawrence Zitnick, and Ross Girshick. Clevr: A diagnostic dataset for compositional language and elementary visual reasoning. In *Proceedings of the IEEE Conference on Computer Vision and Pattern Recognition*, pages 2901–2910, 2017.
- [54] Oliver Groth, Fabian B Fuchs, Ingmar Posner, and Andrea Vedaldi. Shapestacks: Learning vision-based physical intuition for generalised object stacking. In *Proceedings of the European Conference on Computer Vision (ECCV)*, pages 702–717, 2018.
- [55] Lawrence Hubert and Phipps Arabi. Comparing partitions. *Journal of Classification*, 2(1):193–218, December 1985. ISSN 1432-1343. doi: 10.1007/BF01908075.
- [56] Pablo Arbelaez, Michael Maire, Charless Fowlkes, and Jitendra Malik. Contour detection and hierarchical image segmentation. *IEEE transactions on pattern analysis and machine intelligence*, 33(5):898–916, 2010.
- [57] Leon Gatys, Alexander Ecker, and Matthias Bethge. A Neural Algorithm of Artistic Style. *Journal of Vision*, 16(12):326–326, August 2016. ISSN 1534-7362. doi: 10.1167/16.12.326. Publisher: The Association for Research in Vision and Ophthalmology.
- [58] Francesco Locatello, Gabriele Abbati, Thomas Rainforth, Stefan Bauer, Bernhard Schölkopf, and Olivier Bachem. On the fairness of disentangled representations. In *Advances in Neural Information Processing Systems*, pages 14611–14624, 2019.
- [59] Sjoerd Van Steenkiste, Francesco Locatello, Jürgen Schmidhuber, and Olivier Bachem. Are disentangled representations helpful for abstract visual reasoning? *arXiv preprint arXiv:1905.12506*, 2019.
- [60] Frederik Träuble, Elliot Creager, Niki Kilbertus, Francesco Locatello, Andrea Dittadi, Anirudh Goyal, Bernhard Schölkopf, and Stefan Bauer. On disentangled representations learned from correlated data. *arXiv preprint arXiv:2006.07886*, 2020.
- [61] Muhammad Waleed Gondal, Manuel Wüthrich, Djordje Miladinović, Francesco Locatello, Martin Breidt, Valentin Volchkov, Joel Akpo, Olivier Bachem, Bernhard Schölkopf, and Stefan Bauer. On the transfer of inductive bias from simulation to the real world: a new disentanglement dataset. In *Advances in Neural Information Processing Systems*, 2019.
- [62] Andrea Dittadi, Frederik Träuble, Francesco Locatello, Manuel Wüthrich, Vaibhav Agrawal, Ole Winther, Stefan Bauer, and Bernhard Schölkopf. On the Transfer of Disentangled Representations in Realistic Settings. In *International Conference on Learning Representations*, 2021.
- [63] Milton Llera Montero, Casimir JH Ludwig, Rui Ponte Costa, Gaurav Malhotra, and Jeffrey Bowers. The role of disentanglement in generalisation. In *International Conference on Learning Representations*, 2021.
- [64] Babak Esmaeili, Hao Wu, Sarthak Jain, Alican Bozkurt, N Siddharth, Brooks Paige, Dana H. Brooks, Jennifer Dy, and Jan-Willem van de Meent. Structured disentangled representations. In Kamalika Chaudhuri and Masashi Sugiyama, editors, *Proceedings*

of the *Twenty-Second International Conference on Artificial Intelligence and Statistics*, volume 89 of *Proceedings of Machine Learning Research*, pages 2525–2534. PMLR, 16–18 Apr 2019.

- [65] Martin Engelcke, Oiwi Parker Jones, and Ingmar Posner. Reconstruction bottlenecks in object-centric generative models. *arXiv preprint arXiv:2007.06245*, 2020.
- [66] Klaus Greff, Antti Rasmus, Mathias Berglund, Tele Hao, Harri Valpola, and Jürgen Schmidhuber. Tagger: Deep Unsupervised Perceptual Grouping. *Advances in Neural Information Processing Systems*, 29, 2016.
- [67] Sjoerd Van Steenkiste, Michael Chang, Klaus Greff, and Jürgen Schmidhuber. Relational neural expectation maximization: Unsupervised discovery of objects and their interactions. *arXiv preprint arXiv:1802.10353*, 2018.
- [68] Sindy Löwe, Klaus Greff, Rico Jonschkowski, Alexey Dosovitskiy, and Thomas Kipf. Learning object-centric video models by contrasting sets. *arXiv preprint arXiv:2011.10287*, 2020.
- [69] Qian Huang, Horace He, Abhay Singh, Yan Zhang, Ser Nam Lim, and Austin R Benson. Better set representations for relational reasoning. *Advances in Neural Information Processing Systems*, 33, 2020.
- [70] Nicolas Le Roux, Nicolas Heess, Jamie Shotton, and John Winn. Learning a generative model of images by factoring appearance and shape. *Neural Computation*, 23(3):593–650, 2011.
- [71] Anirudh Goyal, Alex Lamb, Jordan Hoffmann, Shagun Sodhani, Sergey Levine, Yoshua Bengio, and Bernhard Schölkopf. Recurrent independent mechanisms. *arXiv preprint arXiv:1909.10893*, 2019.
- [72] Sjoerd van Steenkiste, Karol Kurach, Jürgen Schmidhuber, and Sylvain Gelly. Investigating object compositionality in generative adversarial networks. *Neural Networks*, 130:309–325, 2020.
- [73] Mickaël Chen, Thierry Artières, and Ludovic Denoyer. Unsupervised object segmentation by redrawing. In H. Wallach, H. Larochelle, A. Beygelzimer, F. d'Alché-Buc, E. Fox, and R. Garnett, editors, *Advances in Neural Information Processing Systems*, volume 32. Curran Associates, Inc., 2019.
- [74] Yanchao Yang, Yutong Chen, and Stefano Soatto. Learning to manipulate individual objects in an image. In *Proceedings of the IEEE/CVF Conference on Computer Vision and Pattern Recognition*, pages 6558–6567, 2020.
- [75] Thomas Kipf, Elise van der Pol, and Max Welling. Contrastive learning of structured world models. *arXiv preprint arXiv:1911.12247*, 2019.
- [76] Evan Racah and Sarath Chandar. Slot contrastive networks: A contrastive approach for representing objects. *arXiv preprint arXiv:2007.09294*, 2020.

- [77] Zhixuan Lin, Yi-Fu Wu, Skand Peri, Bofeng Fu, Jindong Jiang, and Sungjin Ahn. Improving generative imagination in object-centric world models. In *International Conference on Machine Learning*, pages 6140–6149. PMLR, 2020.
- [78] Danilo Jimenez Rezende and Fabio Viola. Taming vaes. *arXiv preprint arXiv:1810.00597*, 2018.
- [79] Francesco Locatello, Damien Vincent, Ilya Tolstikhin, Gunnar Rätsch, Sylvain Gelly, and Bernhard Schölkopf. Competitive training of mixtures of independent deep generative models, 2018. arXiv:1804.11130.
- [80] Adam Paszke, Sam Gross, Francisco Massa, Adam Lerer, James Bradbury, Gregory Chanan, Trevor Killeen, Zeming Lin, Natalia Gimelshein, Luca Antiga, et al. Pytorch: An imperative style, high-performance deep learning library. *arXiv preprint arXiv:1912.01703*, 2019.
- [81] Martín Abadi, Ashish Agarwal, Paul Barham, Eugene Brevdo, Zhifeng Chen, Craig Citro, Greg S Corrado, Andy Davis, Jeffrey Dean, Matthieu Devin, et al. Tensorflow: Large-scale machine learning on heterogeneous distributed systems. *arXiv preprint arXiv:1603.04467*, 2016.
- [82] Loic Matthey, Irina Higgins, Demis Hassabis, and Alexander Lerchner. dsprites: Disentanglement testing sprites dataset, 2017. URL <https://github.com/deepmind/dsprites-dataset/>.
- [83] SM Ali Eslami, Danilo Jimenez Rezende, Frederic Besse, Fabio Viola, Ari S Morcos, Marta Garnelo, Avraham Ruderman, Andrei A Rusu, Ivo Danihelka, Karol Gregor, et al. Neural scene representation and rendering. *Science*, 360(6394):1204–1210, 2018.
- [84] Chris Burgess and Hyunjik Kim. 3d shapes dataset, 2018. URL <https://github.com/deepmind/3dshapes-dataset>.
- [85] Alexis Jacq and Winston Herring. Neural Transfer Using PyTorch, 2021. URL <https://github.com/pytorch/tutorials>.



## Appendix A. Additional results

In this section, we report additional quantitative results and show qualitative performance on all datasets for a selection of models.

### A.1 Performance in the training distribution

Fig. 10 shows the distributions of the reconstruction MSE and all the segmentation metrics, broken down by dataset and model. The relationship between these metrics is shown more explicitly across models and datasets in Fig. 11.

Fig. 12 shows an overview of downstream factor prediction performance on all labeled datasets (one per row), using either a linear model (left column) or an MLP (right column) as downstream predictor. We report results separately for each object-centric model and for each ground-truth object property. The metric used here is accuracy for categorical attributes and  $R^2$  for numerical attributes. The same plot including the VAE baseline is shown in Fig. 13.

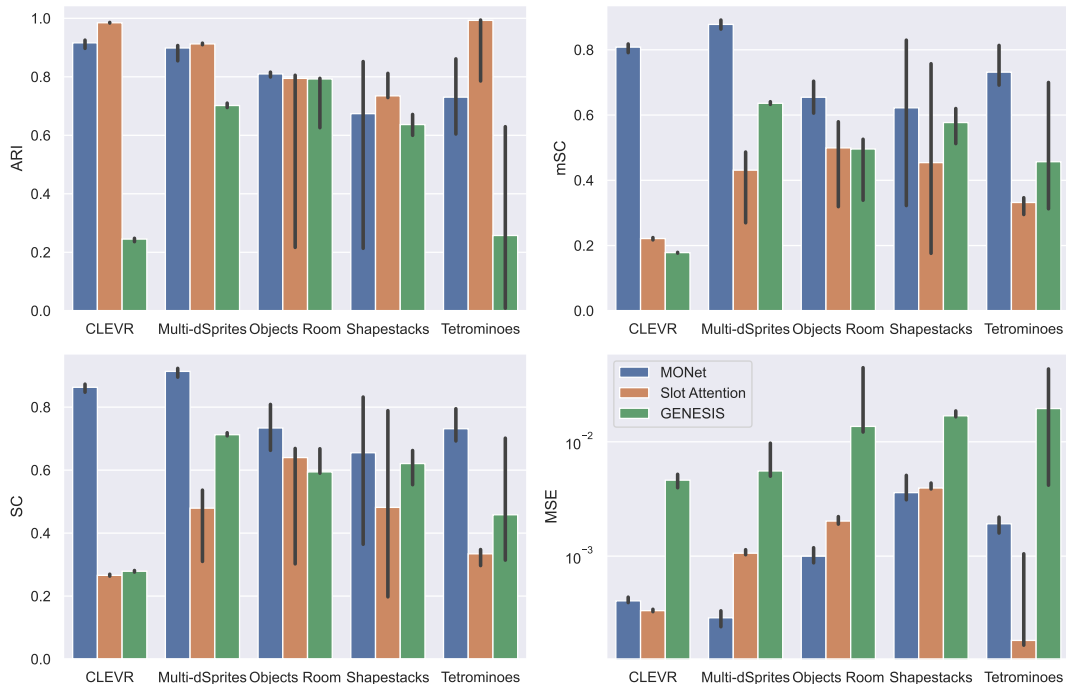


Figure 10: Overview of segmentation metrics (ARI  $\uparrow$ , mSC  $\uparrow$ , SC  $\uparrow$ ) and reconstruction MSE ( $\downarrow$ ) in distribution (test set of 5,000 images). Medians and 95% confidence intervals with 10 random seeds.

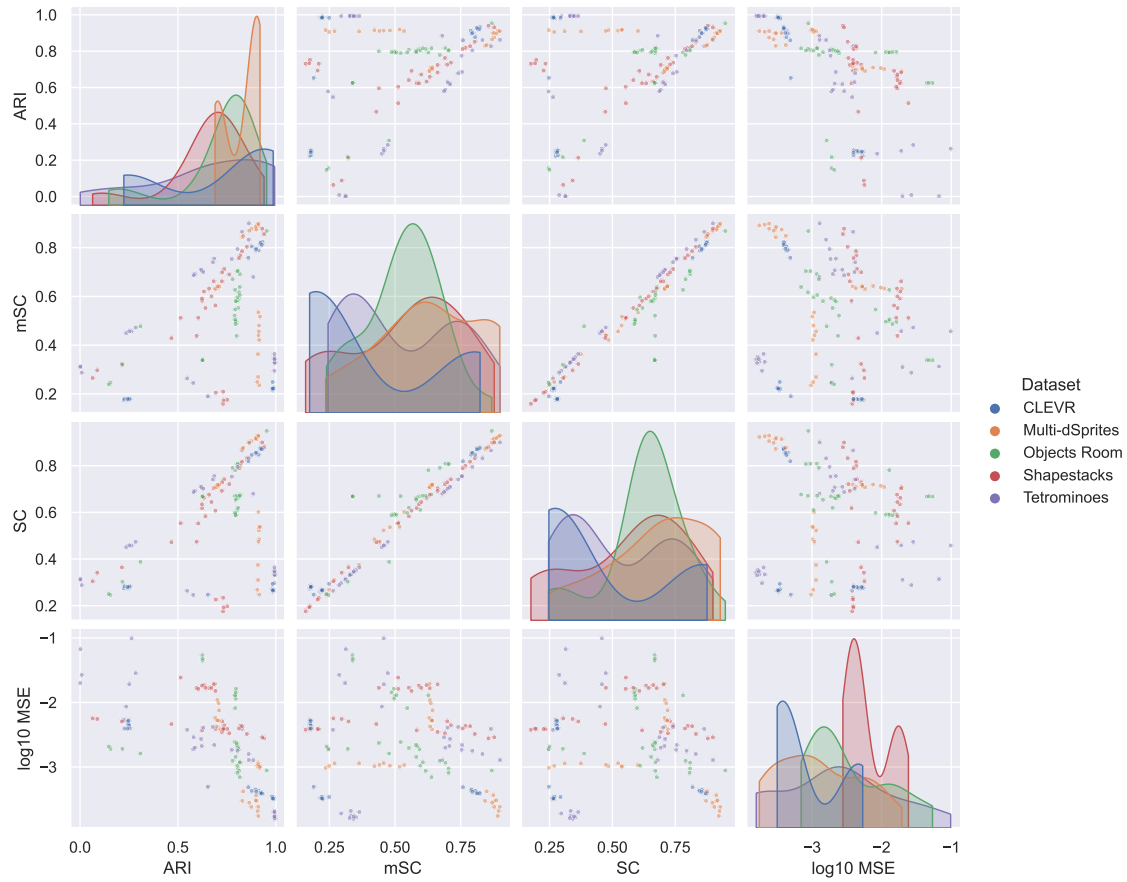


Figure 11: Scatter plots between metrics over all 150 trained models, color-coded by dataset. Diagonal plots: kernel density estimation (KDE) of the data on the x-axis.

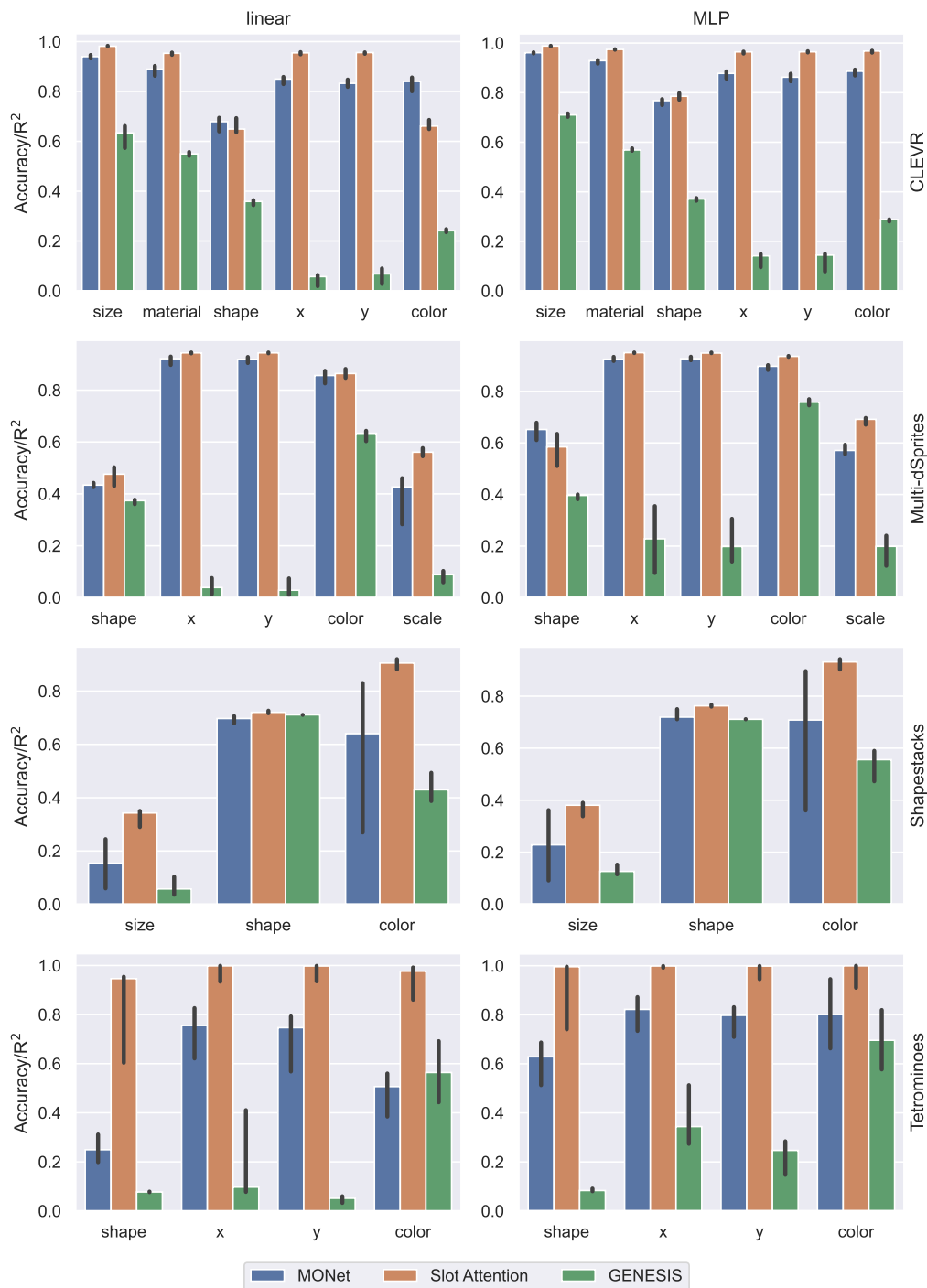


Figure 12: Overview of downstream performance in the training distribution (test set of 5,000 images) for object-centric models. The metrics are accuracy ( $\uparrow$ ) for categorical properties,  $R^2$  ( $\uparrow$ ) for numerical features. The downstream predictors are linear and MLP. Medians and 95% confidence intervals with 10 random seeds.

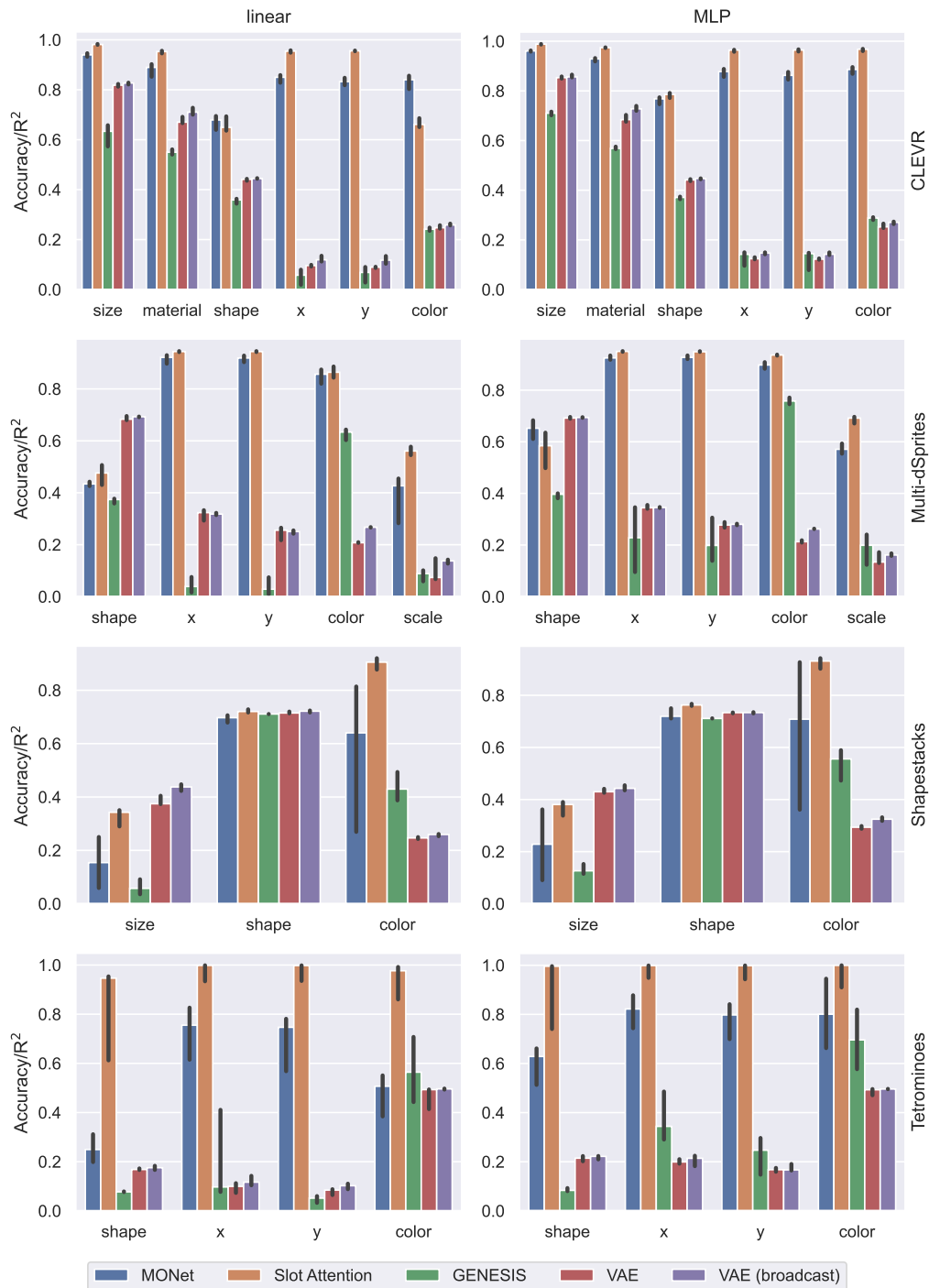


Figure 13: Overview of downstream performance in the training distribution (test set of 5,000 images) for all models, including the baselines. The metrics are accuracy ( $\uparrow$ ) for categorical properties,  $R^2$  ( $\uparrow$ ) for numerical features. The downstream predictors are linear and MLP. Medians and 95% confidence intervals with 10 random seeds.

## A.2 Performance under distribution shifts

### A.2.1 SEGMENTATION AND RECONSTRUCTION

In Fig. 14, we report the distributions of the reconstruction MSE and segmentation metrics in scenarios where one object is out-of-distribution. Results are split by dataset, model, and type of distribution shift, and error bars show standard deviations over 10 random seeds. Fig. 15 shows analogous results when the distribution shift affects global scene properties.

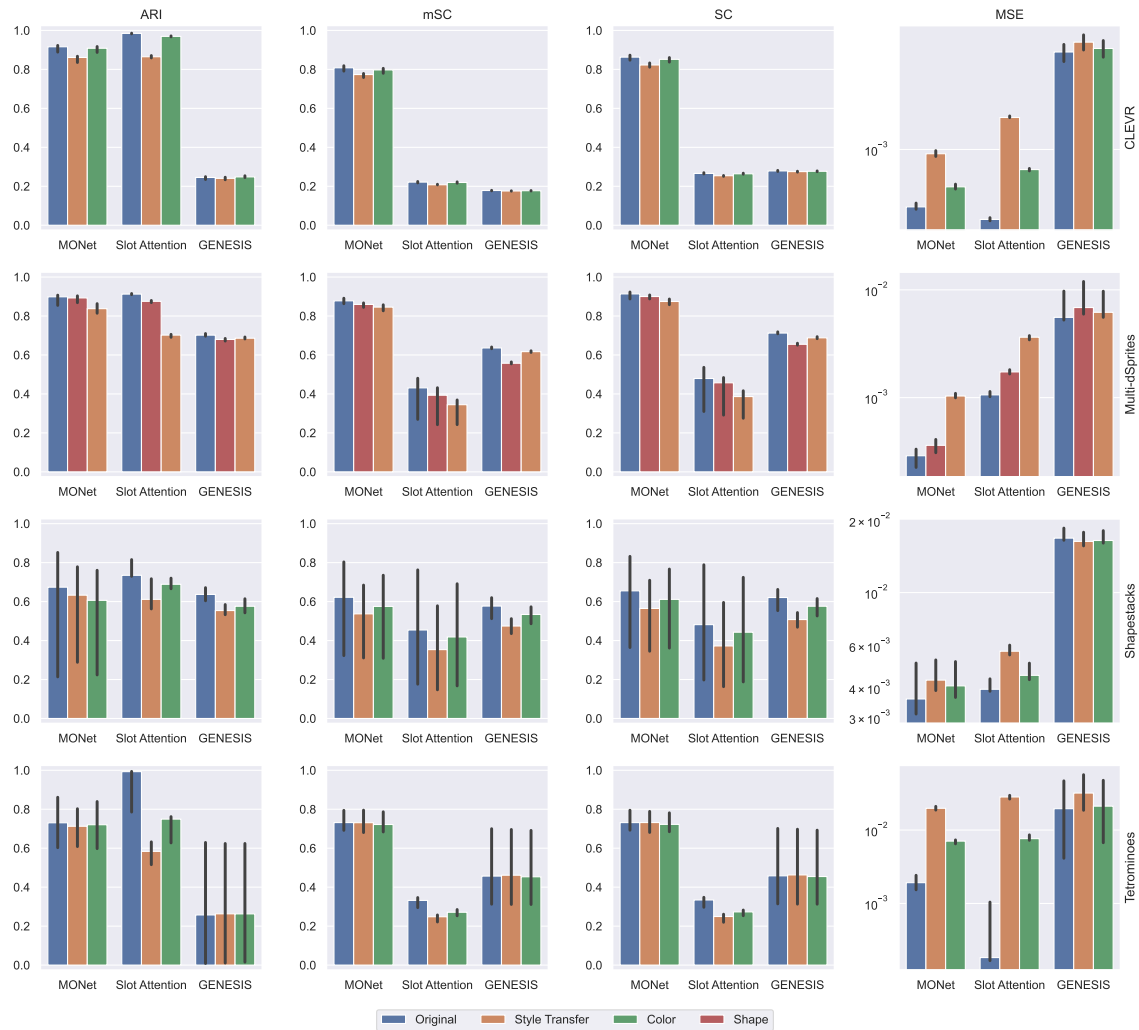


Figure 14: Overview of segmentation metrics (ARI  $\uparrow$ , mSC  $\uparrow$ , SC  $\uparrow$ ) and reconstruction MSE ( $\downarrow$ ) on OOD dataset variants where **one object** undergoes distribution shift (test set of 5,000 images). Medians and 95% confidence intervals with 10 random seeds.

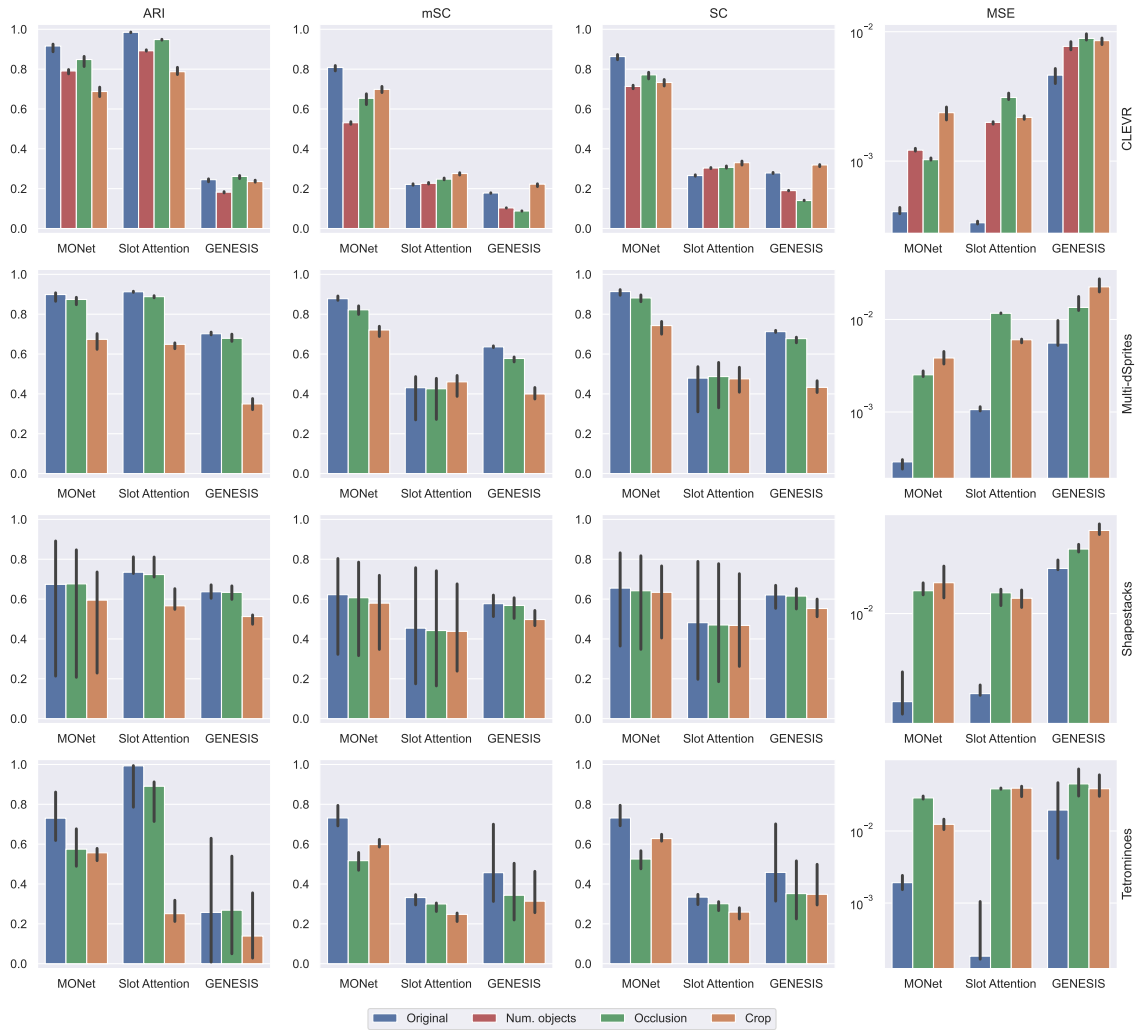


Figure 15: Overview of segmentation metrics (ARI  $\uparrow$ , mSC  $\uparrow$ , SC  $\uparrow$ ) and reconstruction MSE ( $\downarrow$ ) on OOD dataset variants where **global properties** of the scene are altered (test set of 5,000 images). Medians and 95% confidence intervals with 10 random seeds.

## A.2.2 DOWNSTREAM PERFORMANCE

In Fig. 16, we show the relationship between in-distribution and out-of-distribution downstream prediction performance for the same model, dataset, downstream predictor, and object property. We report in separate subplots properties of a different nature (categorical and numerical), and different downstream models (linear and MLP). In the top-left 4 plots, we separately show the average performance of in-distribution (unmodified) and OOD (modified) objects, to highlight the performance degradation on objects that undergo a distribution shift. For unmodified objects, we report the average over the whole scene. Here we observe, as discussed in Section 4.2, that the properties of objects that are still in distribution are still accurately predicted. In all remaining plots, we focus on OOD objects and color-code the results according to dataset, model, or type of distribution shift. Similar results for shifts affecting global scene properties are shown in Fig. 17. Here, the performance drop is similar to the one for OOD objects in the previous case. Figs. 18 and 19 show analogous plots for the case where the downstream model is retrained after the distribution shift. In Figs. 20 and 21, we report similar results comparing object-centric models and baseline VAEs.

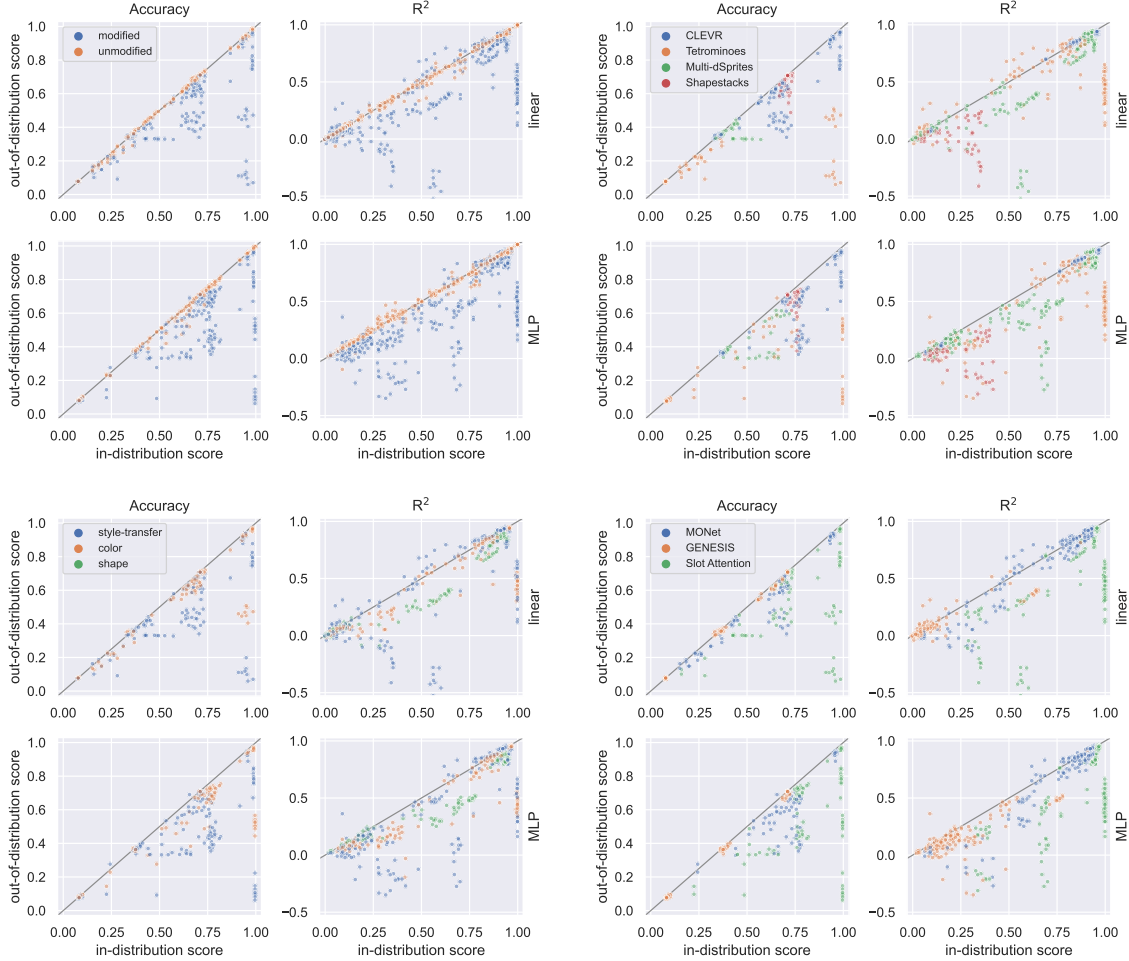


Figure 16: Strong generalization and robustness in downstream prediction. On the x-axis: prediction performance (accuracy or  $R^2$ ) for one object property on one dataset, averaged over the objects in an image. On the y-axis: the same metric in OOD scenarios, where one object undergoes distribution shift. Each data point represents one object-centric model, one object feature, and one type of distribution shift. For each x (performance on one object feature in the training distribution, averaged over objects in a scene) there are multiple y's, corresponding to different distribution shifts. Downstream models are linear (top) or MLP (bottom). In the four plots on the top-left corner, we separately report (color-coded) the performance over in-distribution and OOD objects. In all other plots, we only show OOD objects.



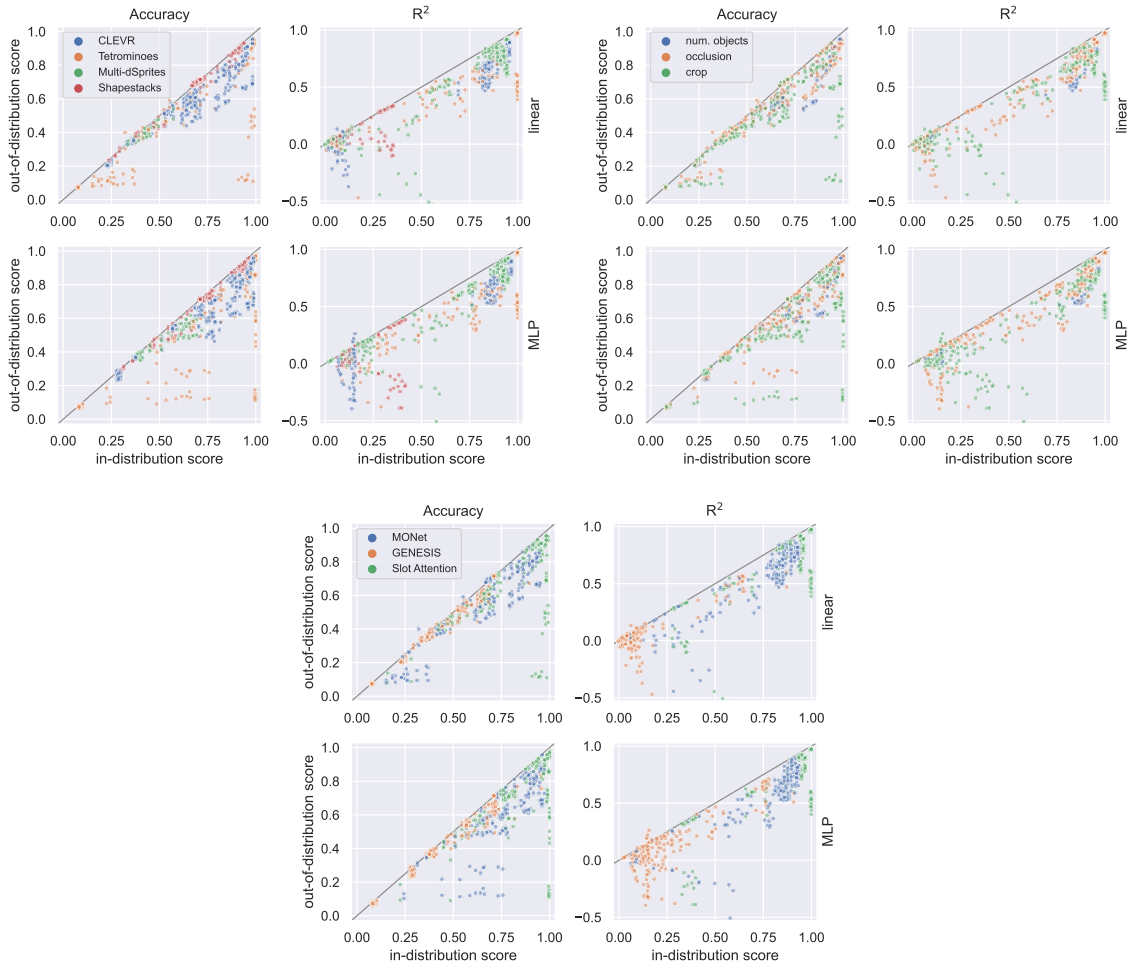


Figure 17: Robustness of downstream prediction to global distribution shifts. On the x-axis: prediction performance (accuracy or  $R^2$ ) for one object property on one dataset, averaged over the objects in an image. On the y-axis: the same metric in OOD scenarios, where global properties of the scene are changed. Each data point represents one object-centric model, one object feature, and one type of distribution shift. For each x (performance on one object feature in the training distribution, averaged over objects in a scene) there are multiple y's, corresponding to different distribution shifts. Downstream models are linear (top) or MLP (bottom).

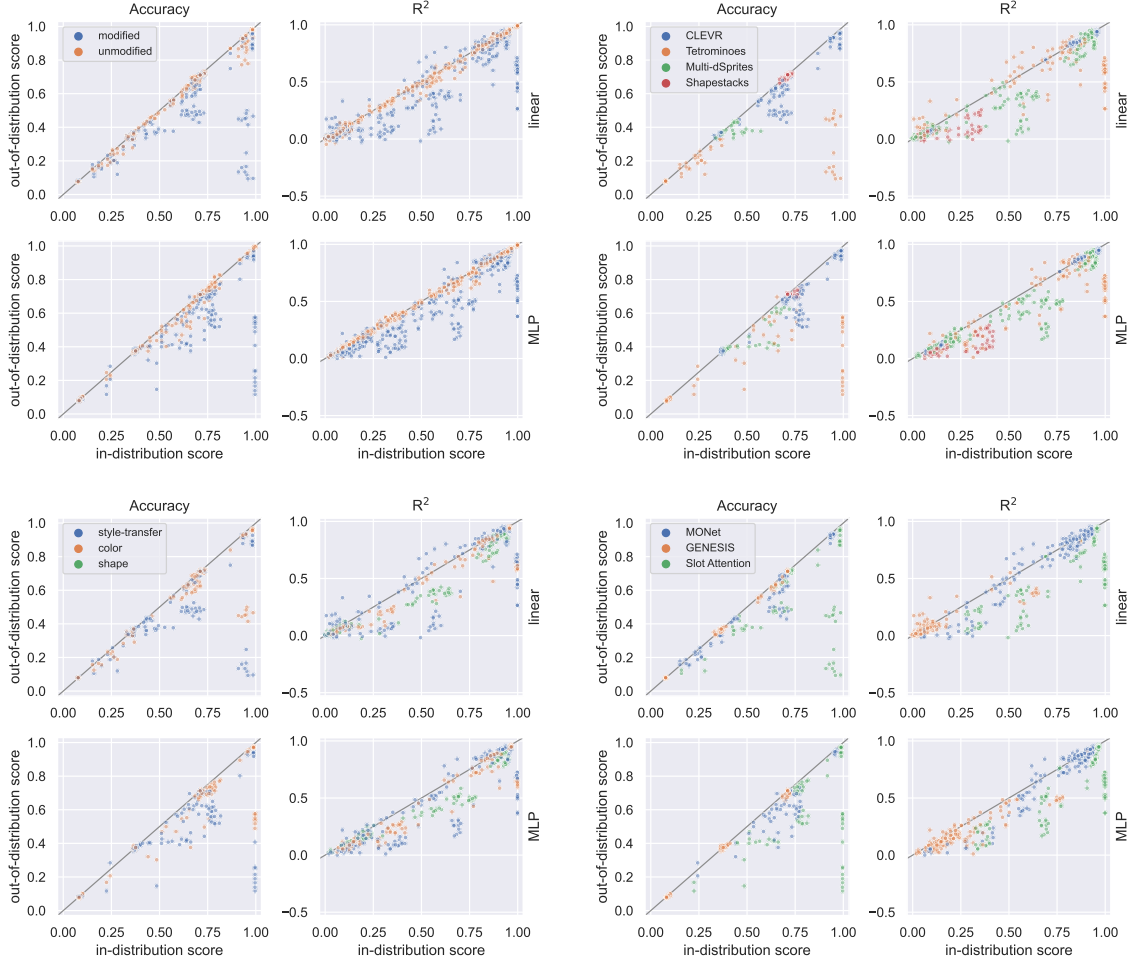


Figure 18: Strong generalization and robustness in downstream prediction, retraining the downstream task after intervention. On the x-axis: prediction performance (accuracy or  $R^2$ ) for one object property on one dataset, averaged over the objects in an image. On the y-axis: the same metric in OOD scenarios, where one object undergoes distribution shift. Each data point represents one object-centric model, one object feature, and one type of distribution shift. For each  $x$  (performance on one object feature in the training distribution, averaged over objects in a scene) there are multiple  $y$ 's, corresponding to different distribution shifts. Downstream models are linear (top) or MLP (bottom). In the four plots on the top-left corner, we separately report (color-coded) the performance over in-distribution and OOD objects. In all other plots, we only show OOD objects.

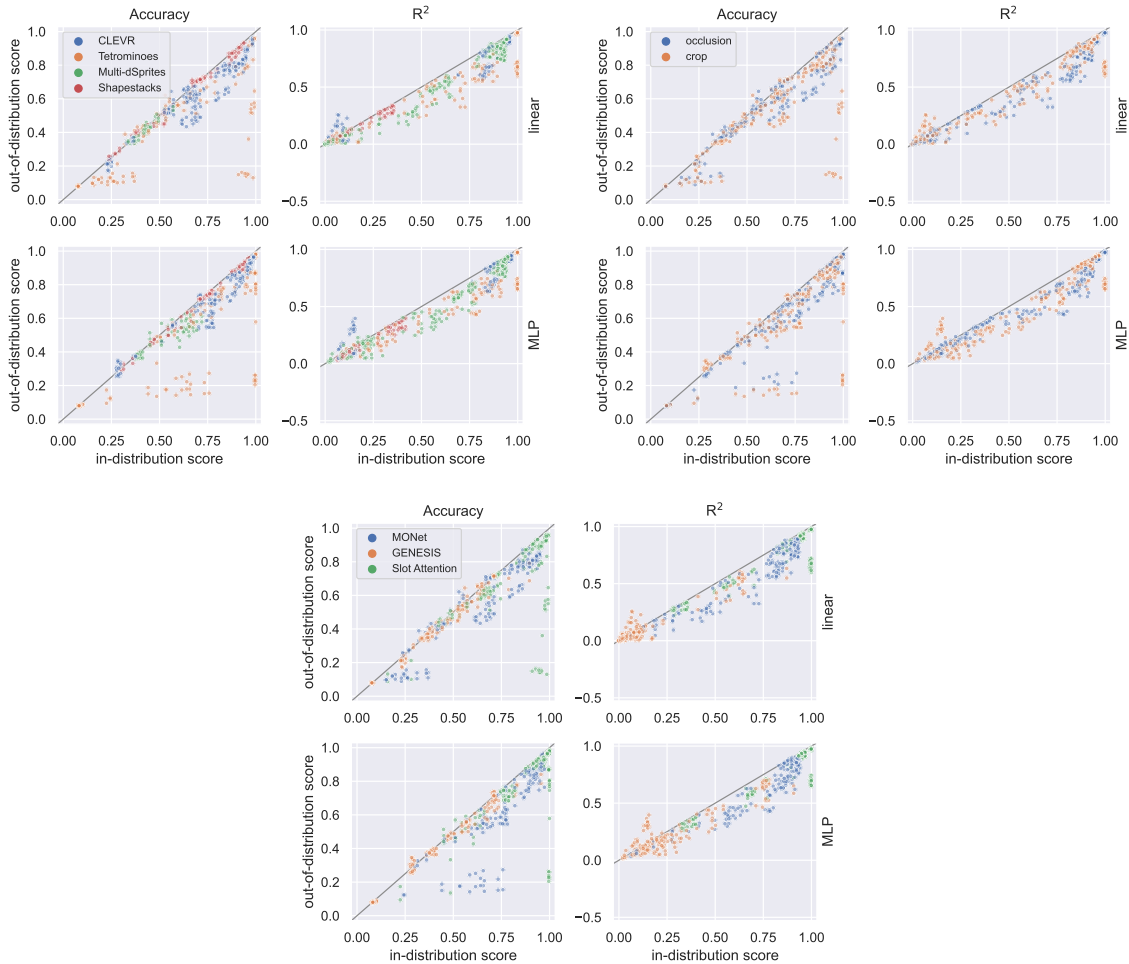


Figure 19: Robustness of downstream prediction to global distribution shifts, when the downstream tasks are retrained. On the x-axis: prediction performance (accuracy or  $R^2$ ) for one object property on one dataset, averaged over the objects in an image. On the y-axis: the same metric in OOD scenarios, where global properties of the scene are changed. Each data point represents one object-centric model, one object feature, and one type of distribution shift. For each x (performance on one object feature in the training distribution, averaged over objects in a scene) there are multiple y’s, corresponding to different distribution shifts. Downstream models are linear (top) or MLP (bottom).

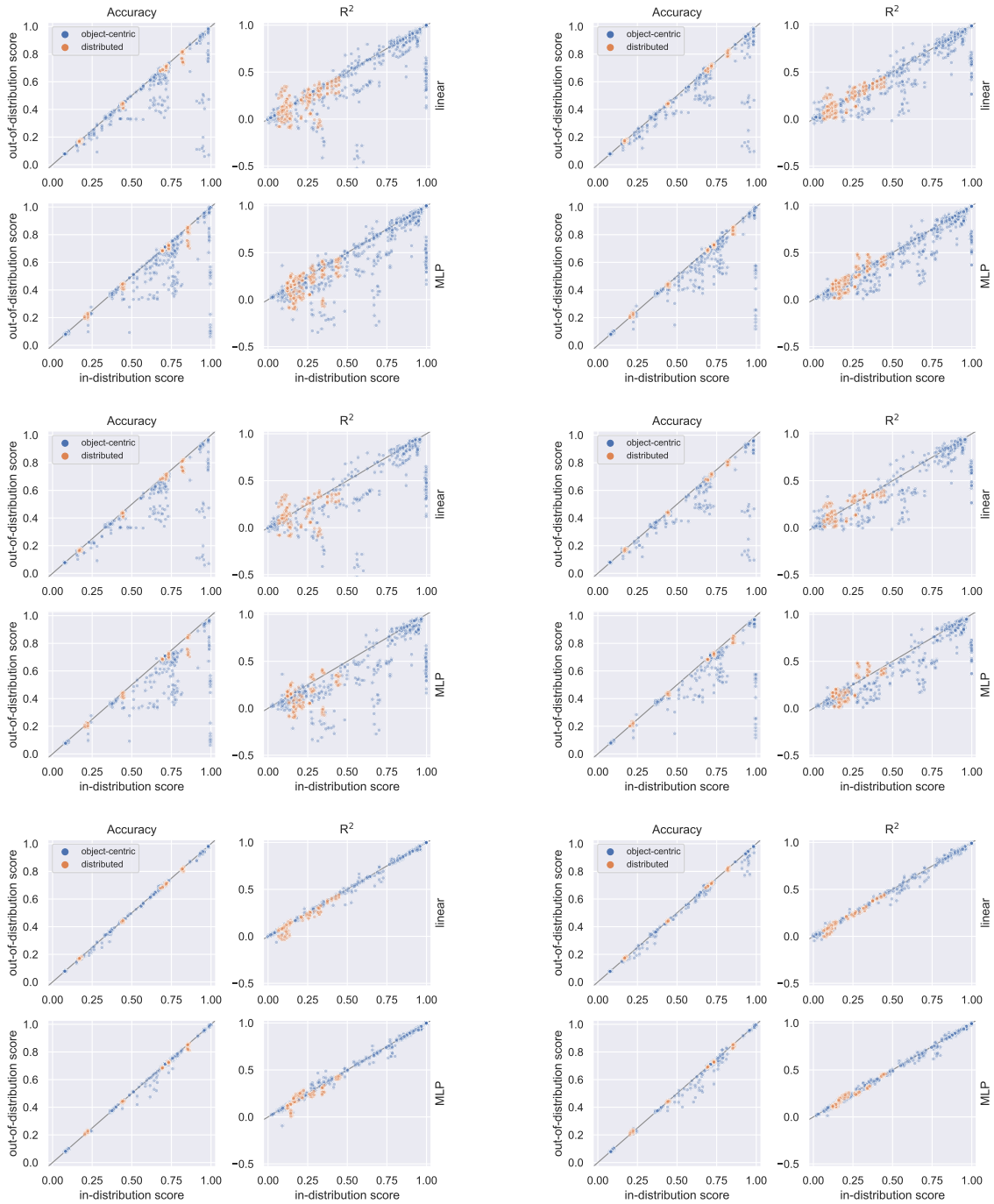


Figure 20: In-distribution vs OOD downstream performance in object-centric and distributed representations, when only one object is OOD. The three rows show, in order: downstream performance on all objects, only on OOD objects, only on in-distribution objects. **Left two columns:** only training downstream models on the original datasets; **Right two columns:** retraining on the OOD datasets.

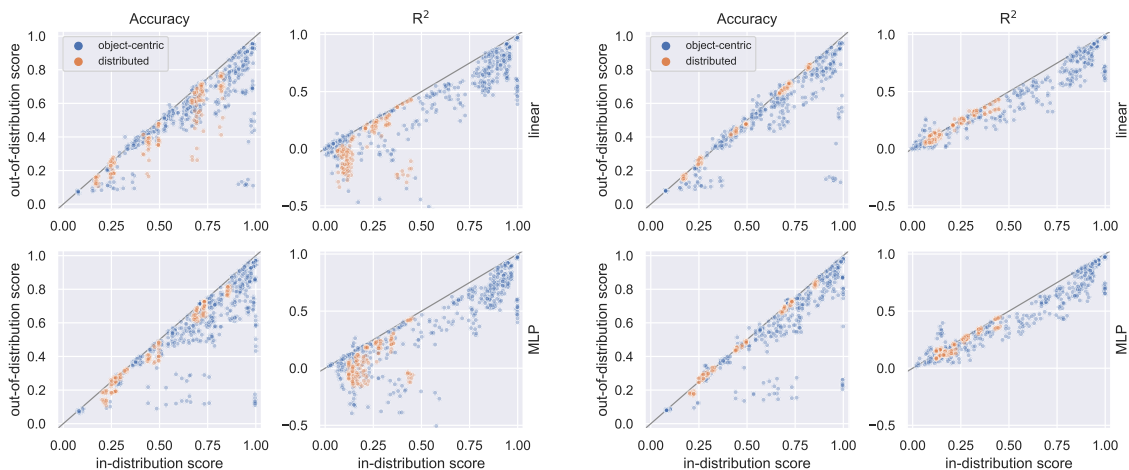


Figure 21: In-distribution vs OOD downstream performance in object-centric and distributed representations, when global properties of the scene are altered. **Left two columns:** only training downstream models on the original datasets; **Right two columns:** retraining on the OOD datasets.

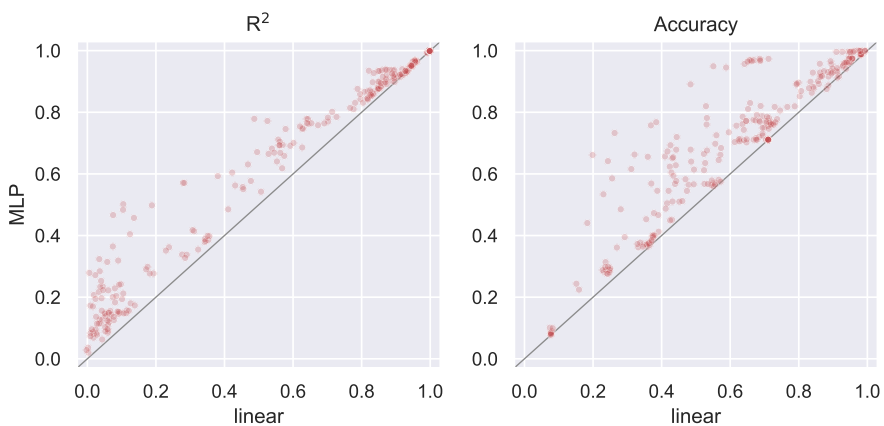


Figure 22: In-distribution downstream performance in property prediction for linear and MLP downstream models. All models, datasets, and object properties are shown here. We separately show the  $R^2$  score ( $\uparrow$ ) for numerical features and accuracy ( $\uparrow$ ) for categorical ones.

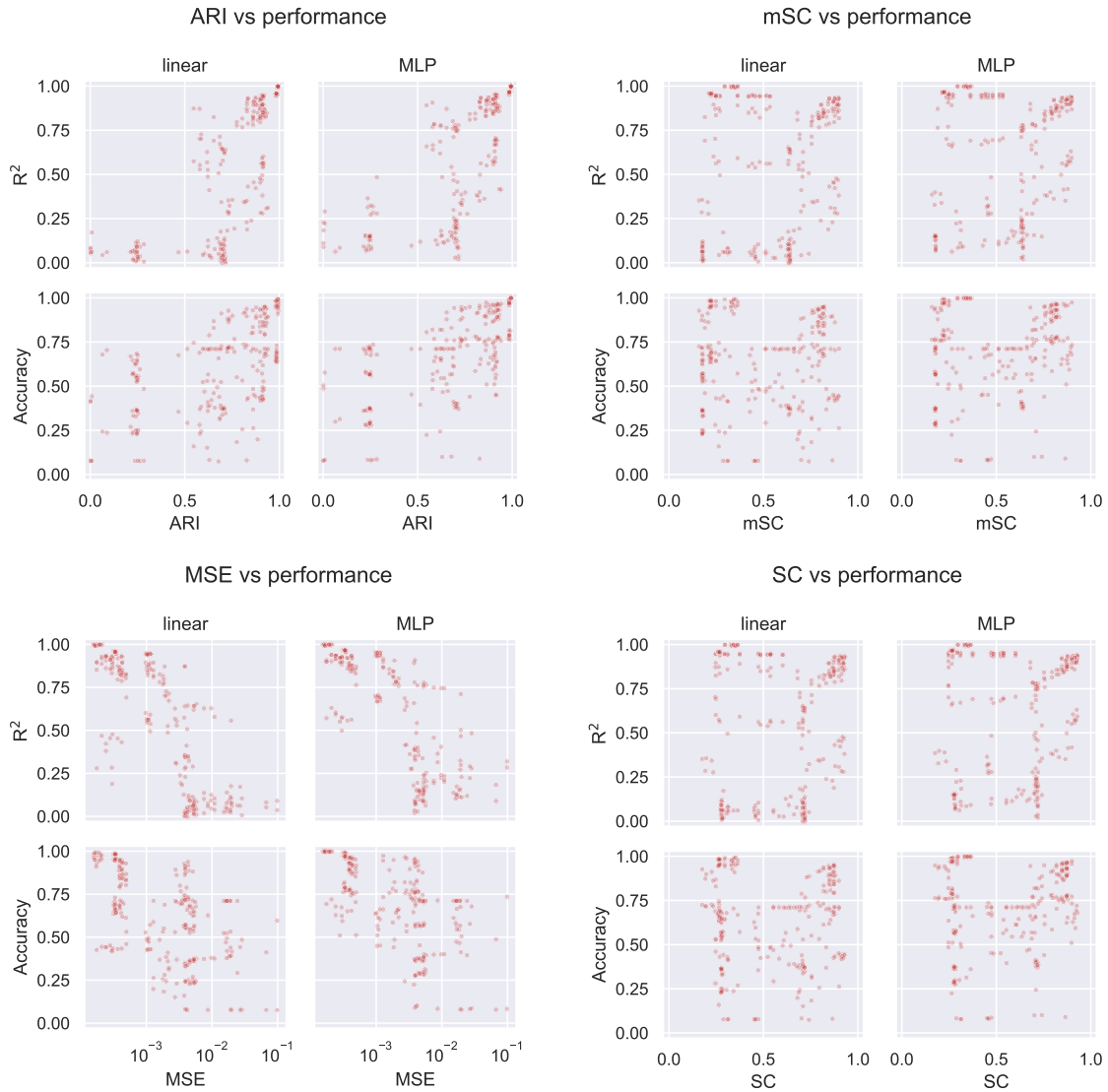


Figure 23: Scatter plots of segmentation metrics (ARI  $\uparrow$ , mSC  $\uparrow$ , SC  $\uparrow$ ) and reconstruction MSE ( $\downarrow$ ) vs. in-distribution downstream performance (accuracy  $\uparrow$  or  $R^2$   $\uparrow$ ). All models, datasets, and object properties are aggregated.

### A.3 Qualitative results

In Figs. 24 to 28 we show the segmentation and reconstruction performance of a random selection of object-centric models on a random subset of test images, for all datasets.

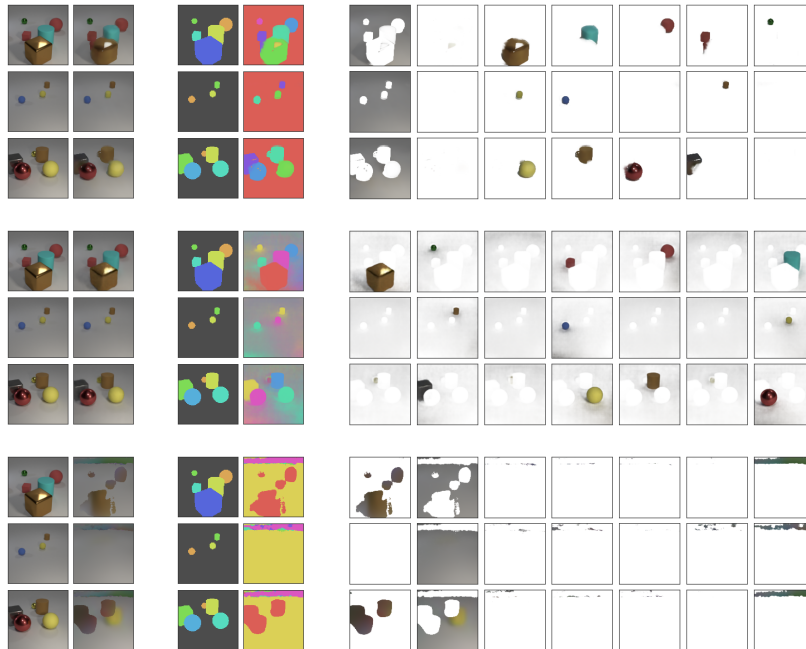


Figure 24: **Segmentation and reconstruction** of 3 random images from **CLEVR6**. Top to bottom: MONet, Slot Attention, GENESIS. Left to right: input, reconstruction, true and predicted (soft) masks, slot-wise reconstructions (masked with the predicted masks).

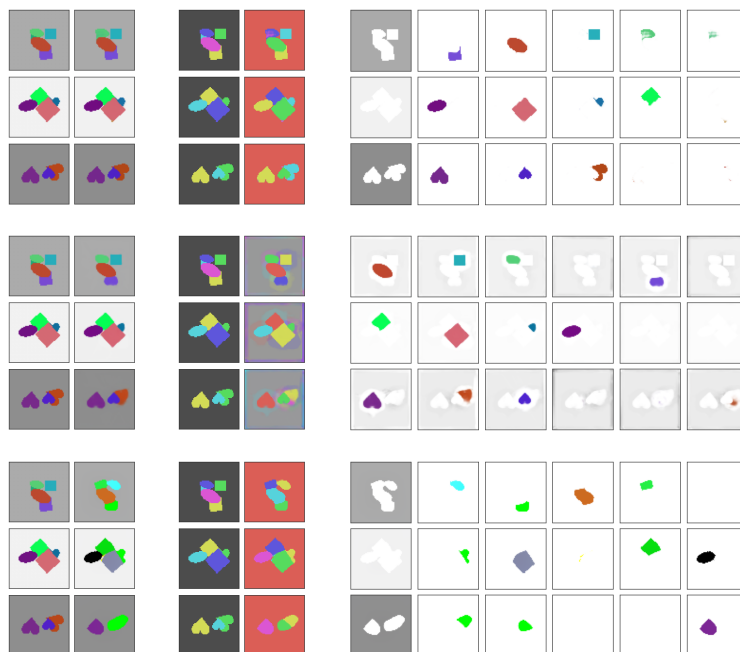


Figure 25: **Segmentation and reconstruction** of 3 random images from **Multi-dSprites**. Top to bottom: MONet, Slot Attention, GENESIS. Left to right: input, reconstruction, true and predicted (soft) masks, slot-wise reconstructions (masked with the predicted masks).

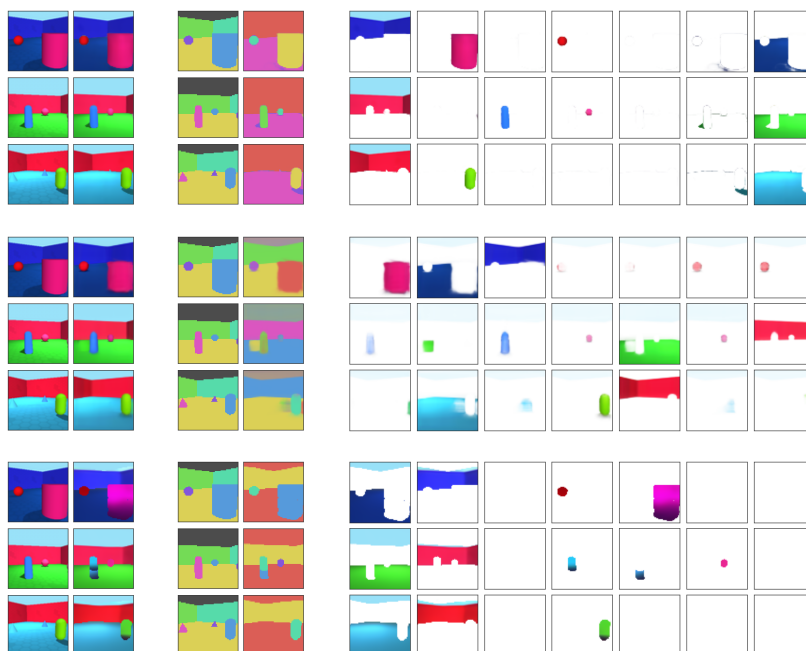


Figure 26: **Segmentation and reconstruction** of 3 random images from **Objects Room**. Top to bottom: MONet, Slot Attention, GENESIS. Left to right: input, reconstruction, true and predicted (soft) masks, slot-wise reconstructions (masked with the predicted masks).



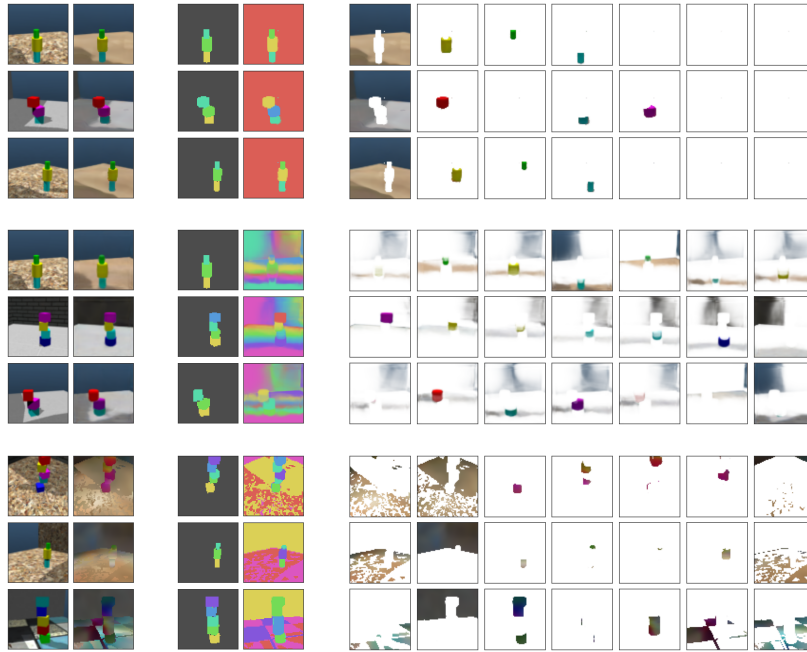


Figure 27: **Segmentation and reconstruction** of 3 random images from **Shapestacks**. Top to bottom: MONet, Slot Attention, GENESIS. Left to right: input, reconstruction, true and predicted (soft) masks, slot-wise reconstructions (masked with the predicted masks).

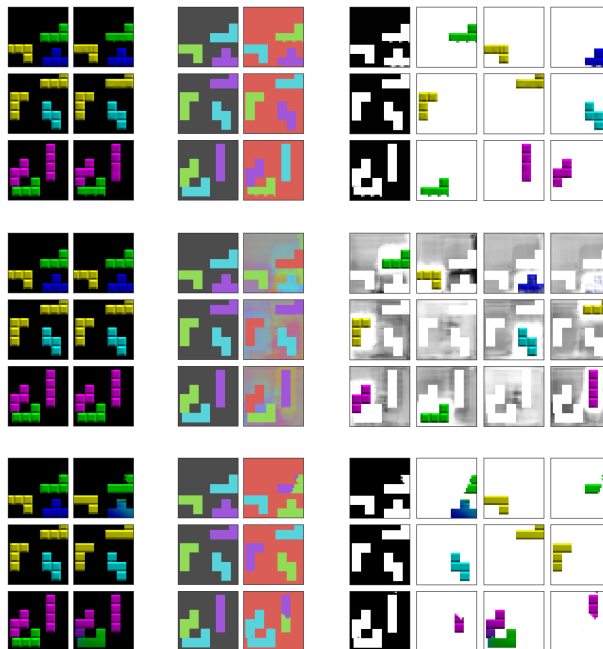


Figure 28: **Segmentation and reconstruction** of 3 random images from **Tetrominoes**. Top to bottom: MONet, Slot Attention, GENESIS. Left to right: input, reconstruction, true and predicted (soft) masks, slot-wise reconstructions (masked with the predicted masks).

## Appendix B. Models

### B.1 Overview

Here we give an overview of the models included in this study. See Fig. 29 for an illustration.

**MONet.** In MONet [11], attention masks are computed by a recurrent segmentation network that takes as input the image and the current *scope*, which is the still unexplained portion of the image. For each slot, a variational autoencoder (the *component VAE*) encodes the full image and the current attention mask, and then decodes the latent representation to an image reconstruction and mask. The reconstructions are combined using the decoded masks into the final reconstructed image. The reconstruction loss is the negative log likelihood of a spatial Gaussian mixture model (GMM) with one component per slot, where each pixel is modeled independently. The overall training loss is a (weighted) sum of the reconstruction loss, the KL divergence of the component VAEs, and an additional mask reconstruction loss for the component VAEs.

**GENESIS.** Similarly to MONet, GENESIS [14] models each image as a spatial GMM. The spatial dependencies between components are modeled by an autoregressive prior distribution over the latent variables that encode the mixing probabilities. From the image, an encoder and a recurrent network are used to compute the latent variables that are then decoded into the mixing probabilities. The mixing probabilities are pixel-wise and can be seen as attention masks for the image. Each of these is concatenated with the original image and used as input to the component VAE, which finds latent representations and reconstructs each scene component. These are combined using the mixing probabilities to obtain the reconstruction of the image. While in MONet the attention masks are computed by a deterministic segmentation network, GENESIS defines an autoregressive prior on latent codes that are decoded into attention masks. GENESIS is therefore a proper probabilistic generative model, and it is trained by maximizing a modification of the ELBO introduced by Rezende and Viola [78].

**Slot Attention.** As our focus is on the object discovery task, we use the autoencoder model proposed in the Slot Attention paper [20]. The encoder consists of a CNN followed by the Slot Attention module, which maps a set of feature vectors into *slots* through an iterative refinement process. At each iteration, dot-product attention is computed with the input vectors as keys and the current slot vectors as queries. The attention weights are then normalized over the slots, introducing competition between the slots to explain the input (cf. also [79]). Each slot is then updated using a GRU that takes as inputs the current slot vectors and the normalized attention vectors. After the refinement steps, the slot vectors are decoded into the appearance and mask of each object, which are then combined to reconstruct the entire image. The model is optimized by minimizing the MSE reconstruction loss. While MONet and GENESIS use sequential slots to represent objects, Slot Attention employs instance slots.

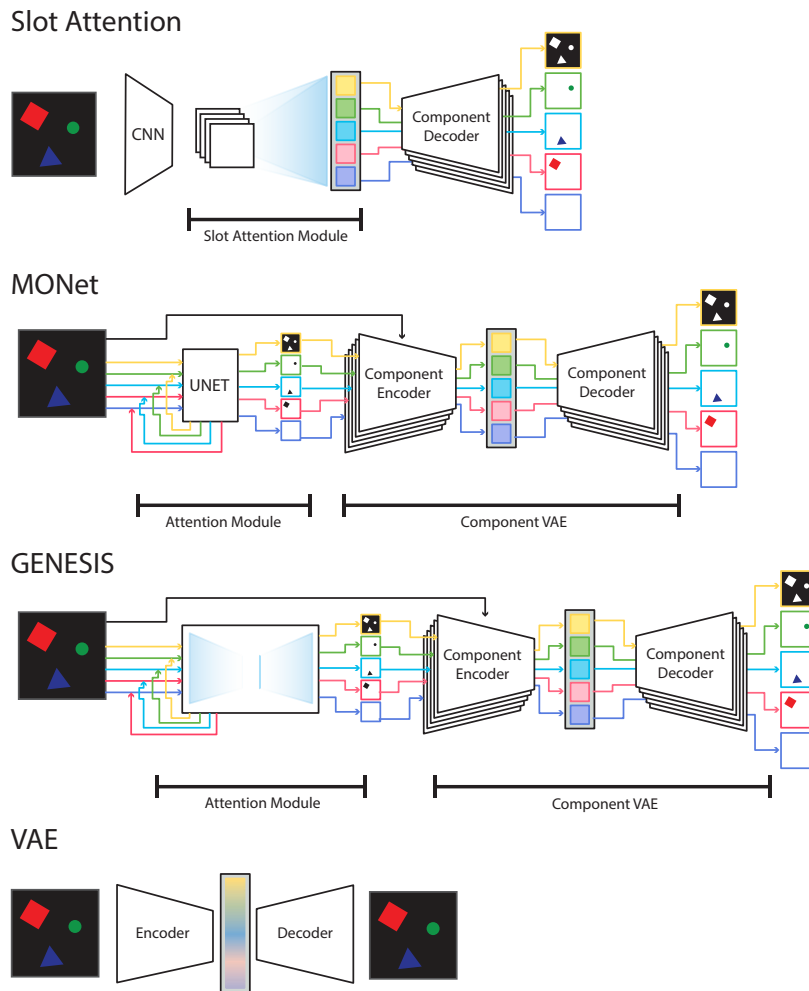


Figure 29: Illustration of the models considered in this study. Different colors in the representations denote separate representational slots in object-centric models. Blurred colors in the latent space of the VAE baselines indicates that the representation is distributed w.r.t. objects, in the sense that there is no inductive bias towards representing objects separately. Component encoders and decoders share parameters across slots: the same encoder is applied independently to each masked input, and the same decoder is applied independently to each slot representation.

**VAE baselines.** We train variational autoencoders (VAEs) [49, 50] as baselines that learn distributed representations. Following Greff et al. [9], we use two different decoder architectures: one consisting of an MLP followed by transposed convolutions, and one where the MLP is replaced by a broadcast decoder [51]. The VAEs are trained by maximizing the usual variational lower bound (ELBO).

## B.2 Implementation details

We implement all models in PyTorch [80]. We re-implement the Slot Attention autoencoder based on the official TensorFlow [81] implementation and the paper [20], and GENESIS based on the official PyTorch implementation. We use the same hyperparameters as defined in the respective publications. We do a best-effort re-implementation of MONet, following the implementation details in the paper [11]. However, a hyperparameter sweep on  $\beta$  and the decoder’s  $\sigma$  parameters was necessary to make this model work satisfactorily on Shapestacks and Tetrominoes—the two datasets where MONet was not originally tested. For GENESIS on Objects Room, we use the same hyperparameters as described in the paper for Multi-dSprites and Shapestacks, which have the same resolution. On CLEVR, which has  $128 \times 128$  images, we use a stride of 2 in the convolutional layer at the middle of both encoder and decoder (the output padding in the decoder is adjusted accordingly). On Tetrominoes, we do the opposite, i.e., we change the first stride in the encoder and the last stride in the decoder from 2 to 1. For Slot Attention on Objects Room and Shapestacks, we use the same parameters used in the original publication for Multi-dSprites, which has the same resolution. For all models, we use a batch size of 64 as in the original publications. On CLEVR, we halve the batch size and the learning rate. In Table 1, we report dataset splits, number of foreground and background objects, and number of slots used when training object-centric models.

The architecture details for the baseline VAE are described in Tables 2 to 4. These are used for the Shapestacks, Multi-dSprites and Objects Room datasets. For CLEVR, an additional `ResBlock` with 64 channels and a `Avg Pool 2D` layer is added at the end of the stack of `ResBlocks`, to downsample the image one more time. This is mirrored in the decoder, where a `ResBlock` with 256 channels and a (bilinear) `Interpolation` layer is added at the beginning of the stack of `ResBlocks`. The same happens in the broadcast decoder case. For Tetrominoes, the number of layers is the same, but the last `Avg Pool 2D` layer is removed from the encoder and the first `Interpolation` layer is removed from the decoder, to have one less downsampling and upsampling, respectively. With these modifications, the number of parameters is comparable across datasets that have images of different sizes. The latent space size is chosen to be  $64 \times$  the number of slots that would be used when training an object-centric model on the same dataset. Note that the number of slots varies depending on the dataset, as shown in Table 1.

Dataset Name	Train Size	Validation Size	Test Size	Background Objects	Foreground Objects	Slots
<i>Multi-dSprites</i>	60000	15000	15000	1	2–5	6
<i>Objects Room</i>	60000	15000	15000	4	1–3	7
<i>Tetrominoes</i>	60000	15000	15000	1	3	4
<i>CLEVR6</i>	40000	7000	6483	1	3–6	7
<i>Shapestacks</i>	60000	15000	15000	1	2–6	7

Table 1: Dataset splits, number of foreground and background objects, and number of slots used when training object-centric models.

<b>Encoder</b>		
<i>Type</i>	<i>Size/Ch.</i>	<i>Notes</i>
Input: $\mathbf{x}$	3	
Conv $5 \times 5$		Stride 2, Padding 2
Leaky ReLU		
Residual Block	64	2 Conv layers
Residual Block	64	2 Conv layers
Conv $1 \times 1$	128	
Avg Pool 2D		Kernel size 2, Stride 2
Residual Block	128	2 Conv layers
Residual Block	128	2 Conv layers
Avg Pool 2D		Kernel size 2, Stride 2
Residual Block	128	2 Conv layers
Residual Block	128	2 Conv layers
Conv $1 \times 1$	256	
Residual Block	256	2 Conv layers
Residual Block	256	2 Conv layers
Flatten		
Leaky ReLU		
Linear	512	
Leaky ReLU		
Layer Norm		

Table 2: Structure of the encoder for both the vanilla and broadcast VAE, excluding the final linear layer that parameterizes  $\mu$  and  $\log \sigma^2$  of the approximate posterior.

<b>Vanilla Decoder</b>		
<i>Type</i>	<i>Size/Ch.</i>	<i>Notes</i>
Input: $\mathbf{z}$	$64 \times$ num. slots	
Leaky ReLU		
Linear	512	
Leaky ReLU		
Unflatten		
Residual Block	256	2 Conv layers
Residual Block	256	2 Conv layers
Conv $1 \times 1$	128	
Interpolation		Scale 2
Residual Block	128	2 Conv layers
Residual Block	128	2 Conv layers
Interpolation		Scale 2
Residual Block	128	2 Conv layers
Residual Block	128	2 Conv layers
Conv $1 \times 1$	64	
Interpolation		Scale 2
Residual Block	64	2 Conv layers
Residual Block	64	2 Conv layers
Interpolation		Scale 2
Leaky ReLU		
Conv $5 \times 5$	Image channels	Stride 1, Padding 2

Table 3: Structure of the decoder for the vanilla VAE.

<b>Broadcast Decoder</b>		
<i>Type</i>	<i>Size/Ch.</i>	<i>Notes</i>
Input: $\mathbf{z}$	$64 \times$ num. slots	
Broadcast	$64 \times$ num. slots +2	Broadcast dim. 8
Residual Block	256	2 Conv layers
Residual Block	256	2 Conv layers
Conv $1 \times 1$	128	
Residual Block	128	2 Conv layers
Residual Block	128	2 Conv layers
Interpolation		Scale 2
Residual Block	128	2 Conv layers
Residual Block	128	2 Conv layers
Conv $1 \times 1$	64	
Interpolation		Scale 2
Residual Block	64	2 Conv layers
Residual Block	64	2 Conv layers
Leaky ReLU		
Conv $5 \times 5$	Image channels	Stride 1, Padding 2

Table 4: Structure of the decoder for the broadcast VAE. One less **Interpolation** is required, because the final image size for this architecture is 64 and the broadcasting is to a feature map of size 8.

## Appendix C. Datasets

We collected 5 existing multi-object datasets and converted them into a common format. *Multi-dSprites*, *Objects Room* and *Tetrominoes* are from DeepMind’s Multi-Object Datasets collection, under the Apache 2.0 license [52]. *CLEVR* was introduced by Johnson et al. [53] and we use segmentation masks from [52]. *Shapestacks* was introduced by Groth et al. [54] under the GPL 3.0 license. We give below an overview of these datasets, and provide further details in the following subsections. See Fig. 30 for sample images and ground-truth segmentation masks for these datasets.

**Multi-dSprites.** This dataset is based on the *dSprites* dataset [82]. Following previous work [9, 20], we use the Multi-dSprites variant with colored sprites on a grayscale background. Each scene has 2–5 objects with random shapes (ellipse, square, heart), sizes (6 discrete values in  $[0.5, 1]$ ), x and y position, orientation, and color (randomly sampled in HSV space). Objects can occlude each other. The intensity of the uniform grayscale background is randomly sampled in each image. Images have size  $64 \times 64$ .

**Objects Room.** This dataset consists of  $64 \times 64$  images of 3D scenes with up to three objects. It is based on the MuJoCo environment used by Eslami et al. [83] and is a multi-object extension of the *3d-shapes* dataset [84]. Since this dataset includes masks but no labels for the object properties, we can use it only to evaluate segmentation performance.

**Tetrominoes.** This dataset consists of  $32 \times 32$  images (cropped from the original  $35 \times 35$  for simplicity) of 3D-textured tetris pieces placed on a black background. There are always 3 objects in a scene, and no occlusions. Objects have different shapes (19 in total), colors (6 fully saturated colors), x and y position.

**CLEVR.** This dataset consists of  $128 \times 128$  images of 3D scenes with up to 10 objects, possibly occluding each other. Objects can have different colors (8 in total), materials (rubber or metal), shapes (sphere, cylinder, cube), sizes (small or large), x and y positions, and rotations. As in previous work [9, 20], we learn object-centric representations on the CLEVR6 variant, which contains at most 6 objects. The CLEVR dataset has been cropped and resized according to the procedure detailed originally by Burgess et al. [11].

**Shapestacks.** This dataset consists of  $64 \times 64$  images of 3D scenes where objects are stacked to form a tower. Each scene is available under different camera views. Object properties are shape (cube, cylinder, sphere), color (6 possible values), size (numerical) and ordinal position in the stack.

### C.1 Multi-dSprites

Each object has the following properties:

- `color` (numerical): 3-dimensional RGB color vector.



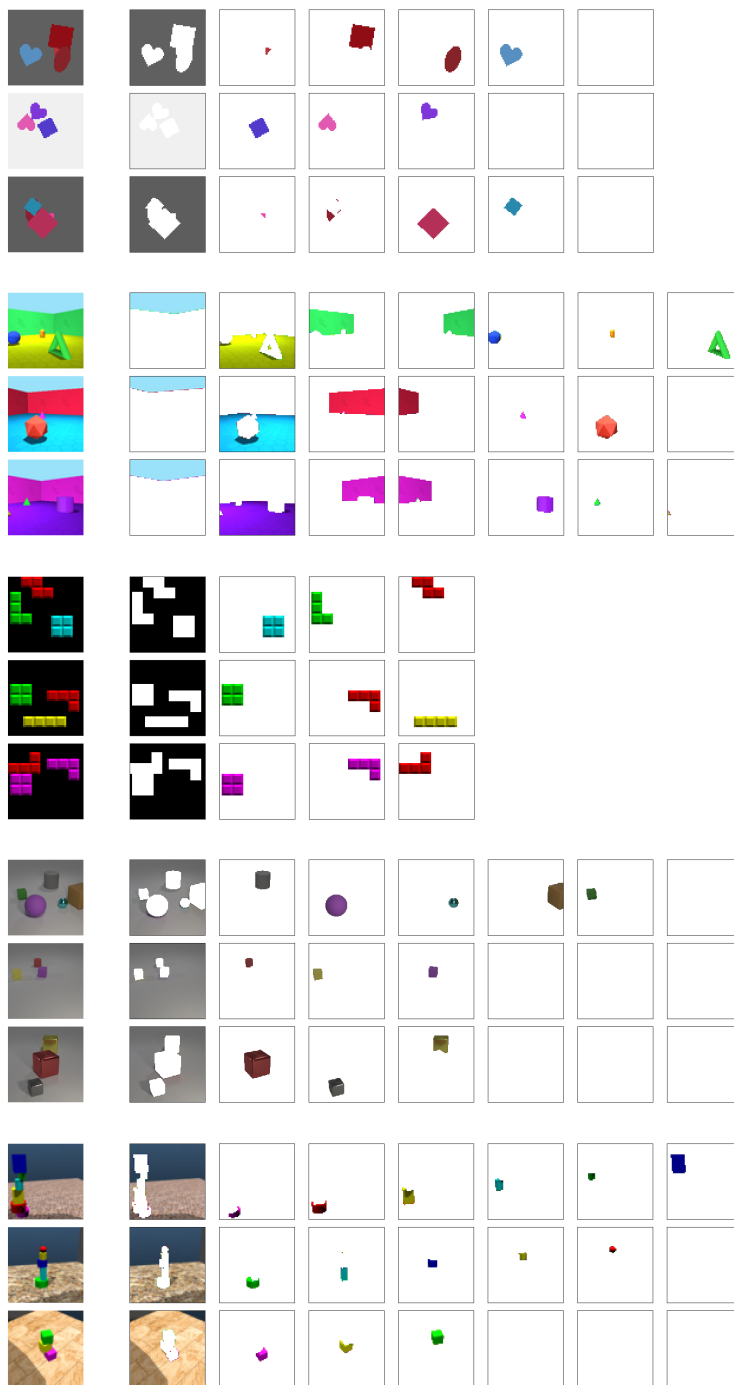


Figure 30: Examples of images from the datasets considered in this work. The left-most column represents the original image, the other columns show all the objects in the scene according to the ground-truth segmentation masks. Top to bottom: Multi-dSprites, Objects Room, Tetrominoes, CLEVR6, Shapestacks.

- **orientation** (numerical): The orientation of the object in radians. The orientation values depend on the shape. This is done taking into account rotational symmetry of the sprites used. The square goes between 0 and  $\frac{\pi}{2}$ , the ellipse between 0 and  $\pi$  and the heart between 0 and  $2\pi$ .
- **scale** (numerical): Scaling of the object, 6 uniformly spaced values between 0.5 and 1.
- **shape** (categorical): The shape type of the object (ellipse, heart, square).
- **x** (numerical): Horizontal position between 0 and 1.
- **y** (numerical): Vertical position between 0 and 1.

## C.2 Tetrominoes

Each object has the following properties:

- **shape** (categorical): 19 shapes:
  - Horizontal I piece.
  - Vertical I piece.
  - L piece pointing downward.
  - J piece pointing upward.
  - L piece pointing upward.
  - J piece pointing downward.
  - L piece pointing left.
  - J piece pointing left.
  - J piece pointing right.
  - L piece pointing right.
  - Horizontal Z piece.
  - Horizontal S piece.
  - Vertical Z piece.
  - Vertical S piece.
  - T piece pointing upward.
  - T piece pointing downward.
  - T piece pointing left.
  - T piece pointing right.
  - O piece.
- **color** (categorical): 6 colors:
  - Blue. RGB:[0, 0, 255]

- Green. RGB:[0, 255, 0]
- Cyan. RGB:[0, 255, 255]
- Red. RGB:[255, 0, 0]
- Purple. RGB:[255, 0, 255]
- Yellow. RGB:[255, 255, 0]
- **x** (numerical): Horizontal position (between 0 and 30).
- **y** (numerical): Vertical position (between 0 and 30).

### C.3 CLEVR

In this dataset, up to 10 objects are placed in a 3D environment. There are 100,000 samples in the full dataset, and 53,483 in the CLEVR6 variant (at most 6 objects). Objects can be occluded by others. On average, 6.2 objects are visible. Each object has the following properties:

- **color** (categorical): 8 colors:
  - Red. RGB:[173, 35, 35]
  - Cyan. RGB:[41, 208, 208]
  - Green. RGB:[29, 105, 20]
  - Blue. RGB:[42, 75, 215]
  - Brown. RGB:[129, 74, 25]
  - Gray. RGB:[87, 87, 87]
  - Purple. RGB:[129, 38, 192]
  - Yellow. RGB:[255, 238, 51]
- **material** (categorical): The material of the object: rubber or metal.
- **shape** (categorical): The shape of the object: sphere, cylinder or cube.
- **size** (categorical): The size of the object: small or large.
- **rotation** (numerical): The rotation of the object, from 0 to  $2\pi$ .
- **x** (numerical): The x coordinate in 3D space.
- **y** (numerical): The y coordinate in 3D space.

## C.4 Shapestacks

Cubes, spheres and cylinders are stacked in a 3D scene and several camera views of the same scene are available. Each object has the following properties:

- **shape** (categorical): shape of the object: cylinder, sphere or cuboid.
- **color** (categorical): 6 colors:
  - Blue. RGB:[0, 0, 255]
  - Green. RGB:[0, 255, 0]
  - Cyan. RGB:[0, 255, 255]
  - Red. RGB:[255, 0, 0]
  - Purple. RGB:[255, 0, 255]
  - Yellow. RGB:[255, 255, 0]
- **size** (numerical): Vector of size 3. For cuboids, these are the lengths of the 3 sides of the object; for cylinders, the first two numbers are the diameter and height, and the third number is 0; for spheres, the first number is the diameter, and the other numbers are 0.
- **coordinates** (numerical): Coordinates in the Euclidean space.
- **level** (categorical): Level of the object in the stack.

## Appendix D. Details on evaluation

### D.1 Segmentation metrics

The Adjusted Rand Index (ARI) [55] can be used to measure the degree of similarity between two sets of segmentation masks. The value of this metric is in  $[-1, 1]$ , it is 0 when one of two sets is made using random label assignments, and 1 when the two sets match (up to label permutation). Segmentation Covering (SC) uses the intersection of union (IOU) between pairs of segmentation masks from the two sets. The masks that have maximal IOU are paired. The value of this metric is in  $[0, 1]$ . While standard (weighted) SC weights the IOU by the size of the ground truth mask, mean (or unweighted) segmentation covering (mSC) gives the same importance to masks of different size. Note that a high SC score can be achieved even when small objects are not segmented correctly. Therefore, mSC is considered to be a more meaningful metric than SC across different datasets [14]. Unlike both segmentation covering metrics, ARI does not penalize over-segmentation of objects into separate slots.

### D.2 Distribution shifts for OOD evaluation

Here we present more in detail the distribution shifts we apply to images in order to test OOD generalization in different scenarios (see examples in Fig. 31).

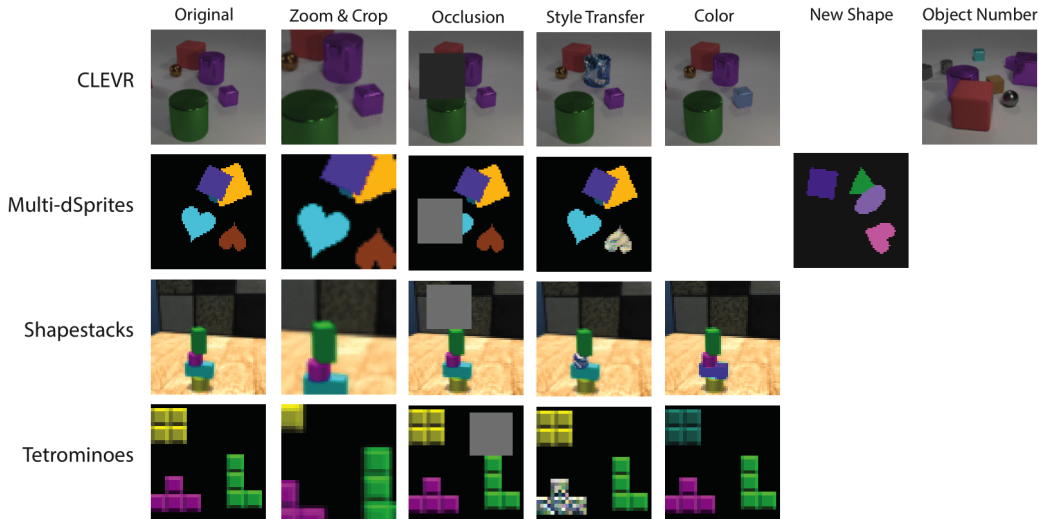


Figure 31: Distribution shifts applied to the different datasets to test generalization and robustness.

**Occlusion.** A gray square is placed on top of the scene. The position is determined by picking 5 locations uniformly at random and selecting the one that occludes less (in terms of total area) of the objects in the foreground. Occluded objects have their mask updated to reflect the occlusion. The color of the square is  $[0.2, 0.2, 0.2]$  for CLEVR and  $[0.5, 0.5, 0.5]$  for all other datasets.

**Color.** This transformation is not performed on multi-dSprites, since the shape colors in this dataset cover the entire color space. An object is selected uniformly at random and their color is changed by performing a random color jittering which changes brightness, contrast, saturation and hue values.

**Crop.** The image is cropped in the center and resized to match its original size. When resizing, we use bilinear interpolation for the image and nearest neighbor for the mask. The objects that have been affected by the cropping have their mask updated.

**Style Transfer.** We implement style transfer based on Gatys et al. [57] and on the PyTorch tutorial in [85]. The first 100k samples in all datasets are converted using as style image *The Great Wave off Kanagawa* from Hokusai’s series *Thirty-six Views of Mount Fuji*. The style is applied only to one foreground object using the object masks. The color and material properties (when relevant) are not used in the training.

**New Shape.** For the multi-dSprites dataset, a triangle is placed on the scene with properties sampled according to the same distributions defined by the multi-dSprites dataset. This is performed only on the images where at most 4 objects are present. The depth of the triangle in the object stack is selected uniformly at random between 1 and 5. All objects from the selected depth and upwards are moved up by one level to place the triangle underneath them. The objects masks are adjusted accordingly for both the added shape and the objects below it.